Spring 2017

CFD evaluation of cluster specific image based asthma lung features on particle transport and hygroscopic particle growth model validation

Lawrence Joseph LeBlanc
University of Iowa

CFD EVALUATION OF CLUSTER SPECIFIC IMAGE BASED ASTHMA LUNG FEATURES ON PARTICLE TRANSPORT AND HYGROSCOPIC PARTICLE GROWTH MODEL VALIDATION

by

Lawrence Joseph LeBlanc

A thesis submitted in partial fulfillment
of the requirements for the Master of Science
degree in Mechanical Engineering in the
Graduate College of
The University of Iowa

May 2017

Thesis Supervisors: Professor Ching-Long Lin
Professor Patrick O'Shaughnessy

Graduate College
The University of Iowa
Iowa City, Iowa

CERTIFICATE OF APPROVAL

_____

MASTER'S THESIS

_____

This is to certify that the Master's thesis of

Lawrence Joseph LeBlanc

has been approved by the Examining Committee for
the thesis requirement for the Master of Science degree
in Mechanical Engineering at the May 2017 graduation.

Thesis Committee: _____
Ching-Long Lin, Thesis Supervisor

_____
Patrick O'Shaughnessy, Thesis Supervisor

_____
James Buchholz

_____
Eric A. Hoffman

To Tess Zernhelt and my parents. Your love provided me the inspiration and encouragement needed to succeed in my undergraduate and graduate educations as well as contributing to making me a better man. This document and my degree would not be possible without you keeping me sane.

ACKNOWLEDGEMENTS

I would like to thank my advisors, Dr. Ching-Long Lin and Dr. Patrick O'Shaughnessy for their endless support and assistance in completing this thesis as well as the other elements of my degree. Dr. Lin's guidance dating back to the final years of my undergraduate education have been instrumental in my desire to obtain a graduate degree. Additionally, I would like to thank Professor James Buchholz and Dr. Eric Hoffman for agreeing to be members of my final examination committee.

In addition, I would like to extend my thanks to Babak Haghighi, Dr. Nariman Jahani, Dr. Shinjiro Miyawaki, Dr. Sanghun Choi, and Dr. Jiwoong Choi for their assistance with learning to operate the CFD and particle tracking code, preparing subject lung images and performing image registration, and assistance with statistical analysis. Finally, I would like to thank Ralph Altmaier for assisting in the creation of the particle growth experiment. His technical lab skills proved invaluable in experimental construction and data collection.

The work associated with this thesis was supported by FDA grant U01-FD005837, NIH grants U01-HL114494, R01-HL112986, S10-RR024738, S10-RR022421 and NIEHS P30 ES05605-11. Experimental lab space was provided by Dr. O'Shaughnessy and The University of Iowa's College of Public Health and Science. Computational work was performed using The University of Iowa's High Performance Computing clusters and the Extreme Science and Engineering Discovery Environment (XSEDE) computing clusters at the Texas Advanced Computing Center (TACC) and San Diego Supercomputer Center (SDSC).

ABSTRACT

Aerosolized drug delivery to the human lungs for asthma treatment has long been studied and yet the relationship between the delivery efficacy and the inter-subject variability due to gender, age, and disease severity remains unclear. A recent imaging-based cluster analysis on a population of asthmatic patients identifies four clusters with distinct structural and functional characteristics. The use of cluster membership to explore inter-subject variability by investigating numerically the air flow and particle transport in representative subjects of the asthmatic clusters on inhalation drug delivery in asthma sub-populations is proposed. Large-eddy simulations using computed tomography (CT)-based airway models were performed with a slow and deep breathing profile corresponding to application of a metered dose inhaler. Physiologically consistent subject specific boundary conditions in peripheral airways were produced using an image registration technique and a resistance network compliance model. Particle simulations and final deposition statistics were calculated for particle sizes ranging from 1–8 μm. The results suggested an emphasis on the importance of airway constriction for regional particle deposition and prominent effects of local features in lobar, segmental, and sub-segmental airways on overall deposition patterns. Asthmatic clusters characterized by airway constriction had an increase in deposition efficiency in lobar, segmental, and sub-segmental airways. Local constrictions produced jet flows that impinged on distal bifurcations and resulted in large inertial depositions. Decreased right main bronchus (RMB) branching angle decreased the fraction of particles ventilated to the right upper lobe (RUL). Cluster-based computational fluid dynamics results demonstrate particle

deposition characteristics associated with imaging based variables that could be useful for future drug delivery improvements.

One method for circumventing low deposition in small airways due to constriction in tracheobronchial airways is through hygroscopic growth of aerosols for inhalation. Hygroscopic materials have an affinity for water and can enlarge in size significantly as they traverse through respiratory tract. Hygroscopic growth has shown promise as a viable drug delivery method for decreasing deposition in the upper tracheobronchial region and increasing drug penetration and retention in small airways. Current models for hygroscopic growth models show promise in predicting steady state final diameter aerosol droplet sizes, but much uncertainty in predicting transient effects exists. This paper discusses in detail one such growth model and modifies it to include realistic spatial temperature and humidity variations associated with the lung. The growth model is simplified through grouping of terms and is then solved using MATLAB ODE 45 solver. The model is compared to experimentally acquired *in vitro* data for validation. The results do not show good agreement with the model, and suggests that additional factors exist that inhibit aerosol droplet growth from commencing immediately upon entering the respiratory tract like is assumed true in literature. This paper briefly hypothesizes for reasons for model and data disagreement and limitations of current growth models.

PUBLIC ABSTRACT

Subject variability has long been a limitation of improved asthma drug delivery. Asthmatic lungs contain a variety of characteristics that are not present in all patients. These characteristics have implications on effectiveness of drug delivery and provide variability challenges for drug development. A new method for characterizing asthma sub-groups subjects into clusters uses CT-image based characteristics in conjunction with clinical information. The clustering allows for simulation of group representative subjects to investigate the mechanics of group specific variables on air and particle transport. The results demonstrate an emphasis on airway constriction for regional deposition. Subjects with constriction had increased deposition in upper airways. Simulation results conclude that cluster structural characteristics based on CT-imaging could be useful for future drug delivery improvements. Airway constriction was found to hinder drug delivery and penetration to the deep portions of the lungs.

A promising method for circumventing airways constriction and allowing greater penetration of drugs into the deep lung is through growing inhaled aerosols through water absorption in the respiratory tract. Current growth models predict steady state final aerosol sizes well, however much uncertainty exists in modeling the transient growth leading up to final size. This paper discusses one such growth model and suggests a method for improving the quality of predictions for lung application. Model results of transient growth do not agree with experimental data suggesting unaccounted factors at play that inhibit growth. This paper discusses current model limitations and the need for improvement for application to pulmonary drug delivery use.

TABLE OF CONTENTS

LIST OF TABLES

LIST OF FIGURES

CHAPTER 1: CFD ANALYSIS OF ASTHMATIC CLUSTER DEFINING FEATURES AS THEY PERTAIN TO AIR AND PARTICLE TRANSPORT

INTRODUCTION

Over 20 million people in the United States of America experienced a form of asthmatic symptoms in 2003, and the disease has been on a steady incline since 1980. Asthma pathophysiology is characterized through chronic airway inflammation, airway narrowing, and airway wall thickening. Clinical symptoms include trouble breathing, wheezing, and coughing (Moorman et al., 2007). Common treatment of asthma is in the form of aerosolized inhaled bronchodilators and corticosteroids which relax muscles and reduce inflammation respectively (Moorman et al., 2007). Drug administration is typically performed via a metered dose inhaler (MDI) or a dry powder inhaler (DPI). Current drug delivery methods are flawed and ineffective, yielding low deposition statistics in the lower tracheobronchial and pulmonary regions as result of inter-subject lung structure variability, delivery device misuse, aerosol size limitations, and inconsistent inspiration patterns (Borgstrom et al., 2006; Byron, 2004; Newman, 2005).

MDIs are the most common inhalers due to portability and accessibility. They combine the medication with a liquefied hydrofluoroalkanes propellant which is dispersed in a controlled aerosolized dose. MDIs are plagued with inefficiencies from incorrect synchronization between device actuation and patient inhalation and losses in the mouthpiece (Byron, 2004; Newman, 2005). DPIs are non-pressurized dry powder mixture that are breath actuated, eliminating the issues with device synchronization, however the dosage and particle size delivered is dependent on the rate of inhalation and can be difficult to achieve reproducibility and may not be suitable for children who cannot achieve high enough flowrates (Byron, 2004; Telko & Hickey, 2005).

Both medication devices produce an aerosol aerodynamic diameter ranging from 2-6 μm (Byron, 2004; Mitchell et al., 2003; Walenga & Longest, 2016). It has been reported that this size range in combination with device disadvantages typically yields large inertial depositional losses in the oropharyngeal regions ranging from 40-80% (Borgstrom et al., 2006; Byron, 2004; Longest et al., 2012; Longest & Hindle, 2012; Newman et al., 1991). Numerous studies have been performed to characterize deposition patterns and distinguish which drug delivery method is more effective, and there is no obvious answer as represented by the broad depositional efficiency range reported in the oropharyngeal region. It is for this reason that the findings in this paper will be based upon inspiration patterns associated with MDIs since they are considered the "gold standard" (Byron, 2004) and most commonly used due to their portability and cheap cost.

It has been stated already that current pharmaceutical aerosol sizes are too large for lower tracheobronchial deposition. Submicron particles have the ability for minimal extrathoracic deposition and greater deep lung penetration (Xi & Longest, 2008). The problem that persists is that nano-sized particles may not deposit and can be exhaled (Heyder et al., 1986; Jaques & Kim, 2000). Recently, many attempts at improving pharmaceutical drug delivery have been focused on creating a dynamic aerosol size through hygroscopic growth. The idea takes advantage of the solubility of many drugs and combines them with the hygroscopicity of salts to create an aerosolized droplet that enlarges when subjected to the extreme humidity conditions associated with the pulmonary system. By being able to control the growth, medication can be engineered to deposit in specified regional locations for more effective treatment (Longest et al., 2010; Longest & Hindle, 2012; Longest & Hindle, 2010; Son et al., 2013; Tian et al., 2010).

Measuring particle transport in the lungs is difficult. There are three main methods for pulmonary particle transport measurement studies: *in vivo*, *in vitro*, and *in silico*. *In vivo*, taking measurements on a living organism, is the most ideal method of measurement. However current *in vivo* techniques do not allow for a high degree of resolution for analysis. Current techniques such as imaging are restricted to evaluating only total lung, and lobar depositional patterns and cannot evaluate at a branch by branch basis. For example, in one study by Kim et al. (1989), it was demonstrated that depositional patterns are correlated to flow patterns by drug inducing asymmetrical constrictions and using images to observe depositional patterns of radio-labeled inhaled particles. While this method does not have fine analytical resolution, it doesn't require replication of physiologically realistic geometries and boundary conditions.

Another method, *in vitro*, involves physical model construction to perform an experiment with. *In vitro* methods circumvent the issue of invasiveness associated with *in vivo* studies, but it is difficult to construct a model that accurately mimics realistic boundary conditions, airway geometry, and regional ventilation (Fadl et al., 2007; Longest et al., 2010; Longest et al., 2011; Longest et al., 2012; Schlesinger et al., 1977; Schlesinger & Lippmann, 1978). In the Schlesinger et al. (1977) study, radio-labeled particles were used in conjunction with an airway cast created from a cadaver lung. The group produced a realistic geometry and repeated measurements with resolution up to the tracheobronchial region without cutting into the cast, however they applied a constant inspiratory flowrate for ventilation and assumed a constant pressure distribution, which are not physiologically realistic.

The final method, *in silico*, involves creating computational fluid dynamics (CFD) and particle transport models for simulation. This method has become prominent as of recently, especially when combined with *in vitro* or *in vivo* studies (Fadl et al., 2007; Longest & Hindle, 2010). Computer models are more robust, allowing individual particle tracking, and can evaluate deposition at a lung, lobar, or branch level (Fadl et al., 2007; Longest et al., 2012; Walenga & Longest, 2016). When combined with imaging techniques such as multiple detector computed tomography (MDCT) and single photon emission computed tomography (SPECT), researchers can recreate unique and accurate boundary conditions, geometries, and regional ventilations (De Backer et al., 2010; Lambert et al., 2011; Miyawaki et al., 2016; Yin et al., 2013). De Backer et al. (2010) demonstrated the need for using subject specific boundary conditions in a study when results showed non-uniform ventilations in the five lobes.

In all the previously mentioned studies, there were three common limitations that existed. *In vivo* studies lack resolution, *in vitro* lacks realistic boundary conditions and inter-subject variability, and *in silico*, depending on the model simplifications made, lack inter-subject variability. The measuring technique applied is highly dependent on identification of the scope of the research. Researchers have been able to solve the problems related to application of realistic boundary conditions, realistic airway geometries and measurement resolution. Combining inter-subject variability with realistic boundary conditions, realistic geometric airways, and high resolution has been recognized as a critical component of further development of drug delivery research (Longest et al., 2011; Longest et al., 2012; Miyawaki et al., 2016). Obtaining inter-subject variability has inherent challenges. The many characteristics that define an

individual's lung physiology are all influential on fluid and particle transport. Factors such as age, weight, height, smoker, non-smoker, and asthmatic, all have a role in dictating the lung makeup and function (Cheng, 2014). Studying a large enough sample size to achieve statistically relevant results for the global population is not practical, if not impossible. Bos et al. (2015) demonstrated this when they studied inhaled antibiotic deposition of patients with cystic fibrosis using patient specific CT based CFD models. They observed, deposition patterns are highly subject specific, and recognized the need for subjects to be classified in groups. Current computational model complexity and computing costs are too large to preform imaging-based studies on large populations, and obtaining enough samples for statistically relevant data is improbable. Using a population averaged geometry is also highly inaccurate because local features relating to structure and function can be averaged out. Therefore, we adopt a novel cluster-based approach to address inter-subject variability via inter-cluster variability. Specifically, the objective of this study is to explore the notion of using the cluster membership to guide inhalation drug delivery in homogeneous asthmatic sub-populations.

Our group (Choi et al., 2017) has developed a multiscale imaging-based cluster analysis (MICA) which sub-divides 248 non-severe and severe asthma subjects into 4 distinct asthmatic clusters using a set of multiscale quantitative computed tomography (QCT), local and global, variables. Structural variables were identified at the segmental airways in 10 local regions and described airway shape, skeleton structure alteration, airway wall thickness, and constriction in regional locations. The local regions included the trachea, right main bronchus (RMB), left main bronchus (LMB), intermediate bronchus (BronInt), left lower lobe trifurcation (TriLLB), and a subset of each of the 5

lobes. Details of branches included in each lobe subset are explained in Choi et al. (2017). Functional variables, including air trapping and image-registration-derived lung-deformation variables, evaluate the lobar and global performance of the lungs. Initially, 57 QCT structural and functional lung variables were identified for cluster analysis. Through statistical analysis, 10 of the 57 QCT variables were identified as major discriminant variables for clustering. The major variables composed of 2 global, 3 lobar, and 5 local. Clustering results were then compared with clinical patient information such as gender, asthma severity, age, and weight to identify cluster association with clinical characteristics.

Subjects in cluster 1 (C1) consisted of younger, non-severe asthmatics with normal airway structure, reversible lung function and increased lung deformation. Subjects in cluster 2 (C2) were mixed between severe and non-severe asthma, with airway narrowing, lung inflammation and reduction in lung deformation. Cluster 3 (C3) was defined by subjects who tended to be females with airway wall thickening, and slightly decreased lung deformation. Finally, cluster 4 (C4) contained severe asthmatic subjects, typically male, with air trapping, reduced lung deformation, and airway narrowing.

The aforementioned cluster membership was used to guide realistic CT-based CFD air and particle transport simulations in selected cluster representative subjects to achieve a level of inter-subject variability never before achieved, and to study the interplays between cluster-specific structural and functional variables on fluid and particle transport. The results will provide a basis for future research on development of improved and personalized treatments for precision medicine.

METHODS

REPRESENTATIVE SUBJECTS FROM CLUSTER ANALYSIS

In the previous cluster analysis with asthmatics by Choi et al. (2017) a total of 57 imaging-based variables were employed, where each imaging variable identified their own unique structural and functional alteration due to asthma. In this study, structural and 2 functional variables were selected as being discriminate features from the 57 variables with regard to sensitivity characterizing fluid and particle transport. The two structural variables are normalized hydraulic diameter (D_h^*) and branching angle in RMB (θ_{RMB}). The functional variables are the determinant of Jacobian, the volume ratio of total lung capacity (TLC) to functional residual capacity (FRC), and air trapping as a percentage at FRC (AirT%). Choi et al. (2017) normalized hydraulic diameter to the average diameter predicted at the trachea for healthy subjects of the same demographics, eliminating inter-subject variability. AirT% is the percentage of residual gas retained in the lungs at expiration (FRC) and is a common characteristic in obstructive lung diseases. The increase of AirT% would lead to decrease of inspiratory capacity (IC), calculated by the subtraction of FRC to TLC.

For each of the clusters, a representative subject was selected that has key features close to the means of their respective clusters. C3 and C4 were female dominant and male dominant, respectively, and they were both severe asthmatic dominant. On the other hand, C1 and C2 had no dominancy for gender. To eliminate gender variability and asthma severity bias in D_h^*constriction analysis, a male non-severe asthma subject was selected from C2. Similarly, a female subject was selected from C1 to have both genders represented by non-severe subjects. As control subjects, one healthy male (HM) subject

and one healthy female (HF) subject were also selected, in consideration of gender dependent characteristics. The key imaging-based features for subject selection were AirT%, IC, TLC, FRC, and D_h^* in sLLL. Constriction is a global characteristic, but regional constriction is used for subject characterization. D_h^* in sLLL was chosen because there was more variation in constriction between clusters. Table 1 summarizes the subject selection features and associated cluster feature means in parenthesis and Fig. 1 summarizes the MICA, clinical and CFD characteristics of each cluster. Lung images were acquired from the University of Pittsburgh and University of Wisconsin, with an approval of each institutional review board, as part of the Severe Asthma Research Program (SARP). Specific acquisition methods and imaging protocols can be found in Choi et al. (2015). Representative subject demographics and quantifiable structural and functional variables for analysis were also presented in Table 1.

AIRWAY GEOMETRIES AND SIMULATION CASES

Subject three-dimensional geometries were constructed using CT images obtained at TLC for each subject. CT geometry consisted of the glottal constriction, trachea, and intra-thoracic central airways up to 6^{th}-7^{th} generations starting from the trachea, counted as generation 0. Additionally, CT unresolved branches were generated using a volume filling method to create anatomically consistent one-dimensional (1D) skeleton tree to terminal bronchioles with diameter, length, and branching angle information (Tawhai et al. 2000; Tawhai et al., 2004). In addition, 6 segmental bronchi major paths beyond the 7^{th} generation were created for analysis of deposition in smaller airways (< 2mm diameter). In all subjects, unresolved branches were generated and attached up to segmental airways if they were not present in the resolved domain. In addition, segmental

airways right bronchi 1, 4, and 10 and left bronchi 1, 4, and 10 were selected for airway path extraction. These segmental airways correspond to 6 path model selection used in other SARP based studies (Castro et al. 2011; Wu et al. 2015) Child branches with the largest diameters were extracted and anatomical asymmetric branching angles were created based on the 1D skeleton data (Tawhai et al., 2004). Fig. 2(a) shows an example of the 3D CT-based geometry with the extracted 6 paths and the whole CT domain (Miyawaki et al., 2016). Fig. 2(b) illustrates one of the 6-paths that extends from G0 to G17 into the RUL. A separate geometry was created for C4 where unresolved branches were generated and attached such that 7 complete airway generations were available globally in addition to the 6 terminal bronchiole paths. This geometric model was created to evaluate results when more branches are available and from here forward will be referred to as the 7-generation model.

Subject CFD inlet flow conditions at PI and mesh characteristics are reported in Table 2. Mesh sizes were determined such that the average distance from the wall to first element was less than 9 units at peak inspiration ($y^+ < 9$). For all subjects the average distance from the wall to the first element was less than 8.8 wall units in the trachea at peak inspiration (PI) and less than 5.7 at half of peak inspiration (PI/2). Variations in mesh size were primarily dependent on subject flow conditions. Subjects with larger Reynolds number (Re) required denser meshes.

FLUID SIMULATION

A large eddy simulation (LES) model was used to model turbulent flows. The method filtered out small eddies and resolved large ones using space averaging. Effect of unresolved turbulent eddies were parameterized using an anisotropic sub-grid scale

(SGS) eddy viscosity model (Vreman, 2004). The governing equations were thus the incompressible filtered Navier-Stokes equations as shown in (1) and (2).

$$\frac{\partial u_i}{\partial x_i} = 0 \tag{1}$$

$$\frac{\partial u_i}{\partial t} + u_j \frac{\partial u_i}{\partial x_j} = -\frac{1}{\rho}\frac{\partial p}{\partial x_i} + (\nu + \nu_T)\frac{\partial^2 u_i}{\partial x_j dx_j} \tag{2}$$

In the above equations, u_j denotes fluid velocity vector in i direction, p is pressure, ρ is fluid density (1.2 kg/m^3), ν is fluid kinematic viscosity (1.5×10^{-5} m^2/s), and ν_T is the SGS eddy viscosity. (1) and (2) were discretized using the characteristic Galerkin approximation coupled with a fractional four step finite element method (Lin et al., 2005). The CFD model was validated by Lin et al. (2009) and Choi et al. (2009).

BOUNDARY CONDITIONS

Boundary conditions were imposed at the supraglottal inlet, airway walls, and distal ends of ending branches. A linear inspiratory flow rate profile, displayed in (3), consistent with one used during inhalation and activation of an MDI was imposed at the inlet from the beginning of inspiration (Longest et al., 2012). Inspiration was characterized as "slow and deep", with time to peak inspiration (T_{PIFR}) achieved after 1.25 seconds. Peak inspiratory flowrate (PIFR) was calculated using IC, T_{PIFR}, and inhalation period (5 seconds) (Longest et al., 2012). PIFR represented peak inspiratory flow rate and t was time. Re was monitored, and a synthetic eddy model (SEM) was activated and applied to the inlet flow to impose necessary artificial turbulent perturbation to the upstream flow prior to the glottal constriction once Re exceeded 460 (Miyawaki & Lin, 2017). No slip conditions were imposed on the airway wall.

$$Q(t) = \frac{PIFR}{T_{PIFR}} t; \quad 0 \le t \le T_{PIFR} \tag{3}$$

Physiologically consistent flow rate distributions were imposed based on registering CT images at TLC and FRC. Local air volume change fractions at the terminal bronchiole level were computed on the matched local lung regions at an acinar scale, and linked to the distal ends of the three-dimensional (3D) airway model through the 1D skeletonized airway model, providing 3D-1D coupled subject specific regional ventilation (Yin et al., 2010; Yin et al., 2013) for the multiscale lung model. A 1D compliant airway resistance model was also included to incorporate dynamic effects of air flow associated with lobar heterogeneous constriction in the CT-unresolved airway branches (Choi et al., 2016).

PARTICLE TRACKING

Lagrangian particle tracking simulations were performed as a post processing step of fluid simulation and the equations are as follows:

$$\frac{\partial u_{pi}}{\partial t} = F_D\left(u_i - u_{pi}\right) + \frac{g_i(\rho_p - \rho)}{\rho_p} \tag{4}$$

$$F_D = \frac{18\mu}{\rho_p D_p^2 C_c}\frac{C_D Re_p}{24} \tag{5}$$

Where F_D was the drag force per mass imposed on the particle, u_i was fluid velocity, u_{pi} was particle velocity, g_i was gravity, ρ_p was particle density, C_D was drag coefficient, and ρ was fluid density defined before (Maxey & Riley, 1983; Morsi & Alexander, 1972; Nowak et al., 2003). Gravitational acceleration was imposed from the apical to basal direction (negative z). C_c represented the Cunningham correction factor defined by (Hinds, 1999), used to correct drag calculations operating between the continuum and molecular regime. D_p was particle aerodynamic diameter and Re_p was the particle Re. Validation for the particle tracking algorithm was performed previously by Miyawaki et

al. (2012). Brownian motion was not considered, and particle simulations were performed for each subject with aerodynamic diameters of 1, 2, 4, and 8 µm. To obtain statistically reliable solutions, 200,000 spherical particles were released at the beginning of inspiration uniformly in a cylindrical shape at the trachea inlet before the glottal constriction. Particle simulation concluded at peak inspiration at which point the number of active particles in the domain was negligible (less than 1% for all cases). Expiration was not considered for this study. To study the effects of more complete airways, particles were released at the trachea inlet for the 7-generation model. To visualize particle deposition in small airways, separate multi-stage particle release simulations were performed with particles being released at 0.4 seconds at each segmental airway (LB1, LB4, LB10, RB1, RB4, and RB10) leading to one of the major 6 paths in C4. C4 was chosen for this analysis based off preliminary deposition results indicating C4 had the most extreme deposition. Release time corresponded to the approximate time duration for particles released at the trachea to reach the segmental airways of the 6 path. Particle sizes were chosen to visualize a gradual change in results and be consistent with typical aerosol drug delivery sizes (Mitchell et al., 2003; Walenga & Longest., 2016). Stokes number (Stk) is used to explain the behavior of particles in a fluid. It is characterized by the ratio of a particle's stopping distance to the characteristic distance of an object. (Hinds 1999). Stk explains the tendency of particles to follow fluid streamlines. The equation for Stk is shown below where D_b is diameter of the current branch and U_{mean} is mean fluid velocity in the current branch.

$$Stk = \frac{\rho_p D_p^2 U_{mean} C_c}{18 \mu D_b} \quad (6)$$

Particle deposition was quantified with deposition fraction, (DF), deposition efficiency (DE), and deposition density (DD). DE was the difference in number of particles entering $(N_{p,ent.})$ a given region and the number of particles exiting $(N_{p,exit})$ the same region, over $N_{p,ent.}$. DF was the regional difference between the $N_{p,ent.}$ and $N_{p,exit}$, over the total number of particles released in the simulation (N_p). Deposition density was the difference between $N_{p,ent.}$ and $N_{p,exit}$ over the surface area (SA) of that region. All particle statistics exclude terminal branches in calculations to avoid imposed outflow boundary condition effects. Particle ventilation fraction was another variable quantified and represents the ratio of particles entering a region over the total number of particles in the simulation.

$$DF = \frac{N_{p,dep}}{N_p} \tag{7}$$

$$DE = \frac{N_{p,dep}}{N_{p,ent}} \tag{8}$$

$$DD = \frac{N_{p,dep}}{SA} \tag{9}$$

Table 1: Overview of representative subject's demographics, representative subject selection cluster features, subject structural variables for findings analysis, and functional variables for findings analysis. Subject representative features display the subject's value and cluster mean for each feature.

	HF	**HM**	**C1**	**C2**	**C3**	**C4**
Demography						
Gender	Female	Male	Female	Male	Female	Male
Age (yrs.)	29	28	20	52	49	51
Weight (kg.)	61.5	99.0	58.6	111.8	85.1	103.0
Asthma Severity	N/A	N/A	Non-severe	Non-severe	Severe	Severe
Features for Representative Subject Selection						
AirT% (Total)	3.1 (5.8)	1.5 (10.7)	0.2 (5.8)	20.7 (8.6)	4.1 (7.8)	42.2 (32.6)
TLC (Liters)	4.3 (3.9)	5.0 (5.3)	3.8 (4.7)	4.7 (3.7)	4.8 (3.6)	5.3 (5.4)
FRC (Liters)	1.8 (1.7)	1.7 (2.2)	0.7 (1.5)	2.1 (1.9)	2.1 (1.6)	3.5 (3.3)
IC (Liters)	2.5 (2.2)	3.4 (3.1)	3.0 (3.2)	2.5 (1.8)	2.7 (2.0)	1.8 (2.1)
D_h^*(sLLL)	0.35 (0.34)	0.38 (0.33)	0.37 (0.34)	0.24 (0.27)	0.43 (0.34)	0.23 (0.28)
Structural Variables for Analysis						
D_h^*(sLLL)	0.35	0.38	0.37	0.24	0.43	0.23
D_h^*(sRUL)	0.34	0.37	0.35	0.24	0.39	0.20
θ_{RMB} (º)	90.0	90.0	94.8	74.8	91.3	67.9
Functional Variables for Analysis						
Jacobian	2.0	2.4	3.3	1.8	1.9	1.4
AirT%	3.1	1.5	0.2	20.7	4.1	42.2

Table 2: Fluid inlet conditions at PI and CFD mesh characteristics for each simulation.

	HF	**HM**	**C1**	**C2**	**C3**	**C4**
CFD Flow Inlet Conditions at Peak Inspiration (PI)						
Q_{PI} (L/min)	50.2	66.7	60.2	50.5	53.3	35.8
Trachea D_h^*	1.17	0.99	0.88	0.94	1.23	0.97
Re	4364	5364	6647	3905	3894	2742
CFD Mesh Characteristics						
Mesh Size (Millions)	9.22	13.01	16.88	9.91	9.19	8.41
y^+_{PI}	8.0	8.0	8.8	7.5	8.1	6.8
$y^+_{PI/2}$	5.0	5.1	5.7	3.9	4.9	3.8

	Cluster 1	Cluster 2	Cluster 3	Cluster 4
Clinical Features	Easy to control symptoms Non-severe asthma	Little inflammation Difficult to control Mix of non-severe and severe subjects	Female dominant Severe asthma Difficult to control symptoms	Male dominant Difficult to control symptoms Severe asthma
Image Features	Reversible lung function Increased lung deformation	Reduced deformation (Jacobian) Reduced RMB bifurcation angle (θ_{RMB}) Airway constriction (D_h*)	Airway wall thickening Reversible lung function No airway constriction (D_h*)	Reduced deformation (Jacobian) Significant air trapping (AirT%) Airway constriction (D_h*) Reduced RMB bifurcation angle (θ_{RMB})
CFD Features	Increased DF Increased DE in generations 1-3 Large Re Increased Stk	Small Re Increased Stk Increased DF Increased DE in generations 2-9	Slightly smaller Re Low Stk Low DF (particle diameter ≥ 2 μm) Low DE in generations 1-8	Small Re Increased Stk Increased DF Increased DE in generations 2-9

Figure 1: Summary of cluster MICA, clinical, and CFD characteristics.

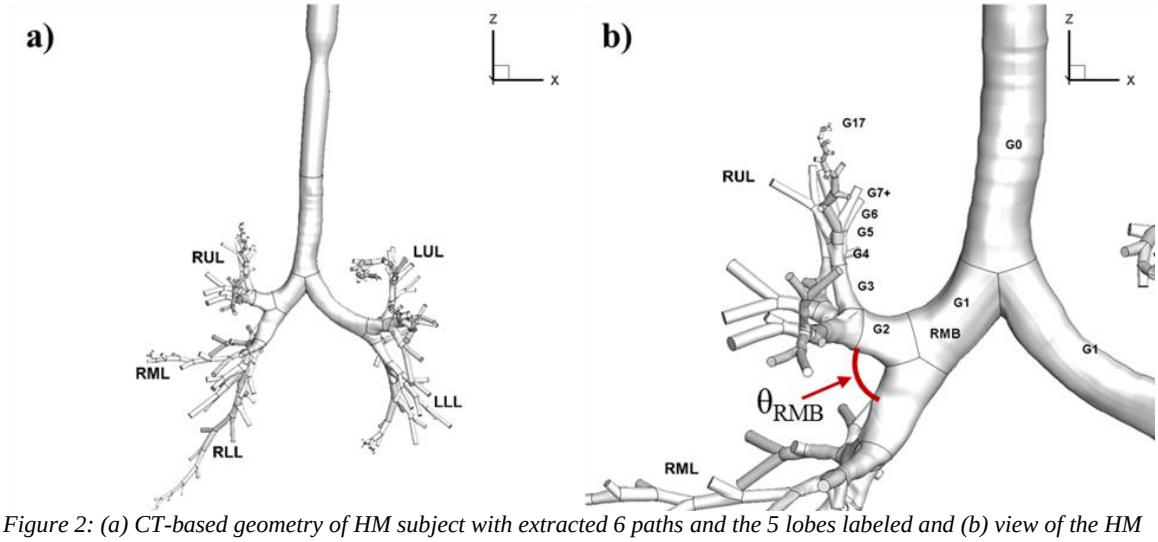

Figure 2: (a) CT-based geometry of HM subject with extracted 6 paths and the 5 lobes labeled and (b) view of the HM subject's LUL with airway generation labels.

RESULTS

FLOW CONDITIONS

Fluid flow characteristics were highly variable between clusters. The generational mean D_h^*, Re, and Stk starting with generation 1 (RMB and LMB) through generation 10 were calculated at peak inspiration and are presented in Fig. 3. For flow information on the trachea (generation 0), see Table 2. C2 and C4 subjects had low initial Re of 2204 and 1947, and small changes in Re from generation 1-10. The C3 subject exhibited a similar pattern with Re decreased from 2448 to 124. This contrasted with HM, HF, and C1 subjects whom all had a large initial Re, and large change in Re. For all subjects, the standard deviation of Re increased with generation, indicating heterogeneous flow characteristics in small airways. At peak inspiration, all subjects except for C1 subject were below the critical Re, defined previously, by the 8^{th} generation.

C2 and C4 subjects had the smallest D_h^* values of all subjects which is consistent with the airway constriction characteristic. Initially, C4 D_h^* was larger than C2, but by generation 3 C4 had the smallest D_h^* values. Small airway classification, defined by branch diameter being less than 2 mm (Cosio Piqueras & Cosio, 2001), was achieved by the 10^{th} generation for HM, C2, and C3 subjects. For C4, small airway classification was not achieved until the 9^{th} generation, and for C1 is beyond the 10^{th} generation.

Average Stk was calculated and plotted for 2 μm and 4 μm particle sizes in Fig. 3. Both particle sizes displayed similar generation trends, but magnitudes differed. The overall Stk trend for all subjects consisted of an increase in Stk through the 6^{th} or 7^{th} generation, and then a sharp decline afterwards. Stk was largest in 5^{th}-7^{th} generations for all subjects and C4 had the greatest Stk values, which were approximately 37% and 27%

larger than C3 at the 6th generation for 2 μm and 4 μm results and approximately 61% larger than C2. C1 and HF initially had large Stk, similar to C4 until the 4th generation. C1 and C3 Stk did not decrease as much in later generations heading into small airway classification.

Subjects in C1 were non-severe and had functional and structural characteristics similar to healthy subjects (Choi et al., 2017). The cluster did not possess any structural characteristics that could be influential on deposition. Due to the dissimilarities to the other asthmatic clusters, for the sake brevity the following deposition results presented will focus on C2, C3, and C4 subjects in detail. Specifically, comparisons will focus on C3 and C4 for their common severe asthma trait and C2 and C4 for their gender, D_h^*, and lung function reduction similarities. For completeness, comparisons between C1 subject and the other asthmatic subjects, and asthmatic subjects with the appropriate healthy gender subject will be made for results deemed important.

For subsequent regional results, lobes were defined as the right upper lobe (RUL), right middle lobe (RML), right lower lobe (RLL), left upper lobe (LUB), and left lower lobe (LLL). Lobar regional ventilation values were plotted in Fig. 4 by lobe, gender, and asthma severity. Blue bars represented healthy subjects, green bars represented non-severe asthma subjects (C1, and C2), and red bars represented severe asthma subjects (C3 and C4). The largest lobar ventilation fractions were in the lower lobes of each lung. HF, C2, C3, and C4 subjects had the greatest lobar flow ventilation fraction in the LLL, while HM and C1 subjects had the greatest fraction in the RLL. For the LUL, LLL, and RML variability between subjects was between 2.2% and 4.9%. For non-severe subjects, regional ventilation was consistent with less than 1% differences in the LLL, LUL, and

RML, but large differences in RUL and RLL as previously mentioned. For the severe asthmatic subjects, C4 (male) had noticeably increased regional ventilation in the RLL and LUL compared to C3. While C3 (female) had increased ventilation in the LLL and RUL.

REGIONAL DEPOSITION

Regional particle ventilation patterns (ratio of particles entering a lobe to total particles released) were also computed and plotted for each lobe in Fig. 5 for 1 μm and 8 μm sized particles which represented the smallest and largest particle sizes. The difference between the two sizes was negligible. The RUL of the healthy female subject had 1.7% difference between 1 μm and 8 μm, which represented the largest particle size difference of all lobes and clusters. The results indicated that ventilation was not sensitive to particle size for the particle size range of interest.

Regional DF in the 5 lobes were calculated and plotted for each subject in Fig. 6 for each particle size. At the large particle sizes (8μm and 4 μm) C2 and C4 subjects had much greater deposition fractions compared to the other clusters, and the differences between those two subjects and the other subjects increased with size. For all particle sizes, there was greater deposition in all lobes in C4 compared to C2 except for the LUL. At small particle sizes, inter-cluster variability was much less and C3 had more similar deposition patterns to C4. In fact, C3 had a larger DF in the RUL and RML. Table 3 shows the upper lobe to lower and middle lobe ratio ($U/(L+M)_p$), and the total whole lung deposition fraction (sum of the lobar fractions). There was a tendency for particles to deposit more in the lower and middle lobes in C4, C3, and C1. Fig. 7 showed the percent difference in total deposition between C4 and HM, C4 and C1, C4 and C2, and C4 and

C3 subjects for the four particle sizes. For the C4 and C2 comparison and C4 and C3 comparison, the percent difference varied by less than ±5% at 1 μm and 2 μm. At large particle sizes, the smallest percent difference was 7.1% between C4 and C2 at 4 μm. Based on low deposition fraction percent difference results, and typical aerosol pharmaceutical drug size ranging from 1-5 μm (Mitchell et al., 2003; Walenga & Longest, 2016), further analysis was limited to results from 2 μm and 4 μm particle sizes.

Average DE by generation was plotted for 2 μm and 4 μm in Fig. 8. Table 4 gives deposition efficiency values at specific generations for comparison of variability between subjects. Subject differences increased with particle size. At 4 μm, C4 and C2 subjects had increased DE in lobar, segmental, and sub-segmental airways (generations 3-6) compared to other subjects. In the 2^{nd}-4^{th} generations, C4 had approximately 30-50% larger DE than C2. In the 5^{th}-7^{th} generations, DE was within 16% of C2. A similar pattern was presented for 2 μm particle DE results. C2 and C4 had increased deposition efficiency in generations 2-5 (lobar, segmental, and sub-segmental) compared to other asthmatic subjects. In generations 2-4, DE in C4 was approximately 25% larger than C2, but at the 5^{th} and 6^{th} generations, DE fluctuated within ±6% of C2.

DE in C4 was much greater than C3. The 1^{st} and 10^{th} generations were the only locations that C3 had a greater DE then C4 for 4 μm results. The differences between the two subjects was largest at generation 4 where C4 had a DE that was 70% larger than C3. Over generations 2-9, DE in C4 was an average of 42% larger than C3. For 2 μm results, DE in C4 was an average of 36% greater in the 2^{nd}-4^{th} airway generations, but less than 2% difference at the 5^{th} and 6^{th} generations. There was a lot more parity between DE of subjects at 2 μm.

To better evaluate deposition in small airways, DE of the C4 multi-stage 6-path particle release simulation results were plotted in Fig. 9. DE was lower in the average of the 6 paths and had less variation compared to the original results. For 2 μm, DE was approximately 57% less in the 4^{th}-6^{th} generations of the multi-stage particle release results, 18% less in generations 8-9, 52% less in generation 10-11, and in generations 12-15, DE fluctuates between 9% greater and 78% less than the original results. For 4 μm, similar comparisons to the trachea release point results were made. DE was approximately 45% less over generations 4-8, with maximum difference occurring at the 6^{th} generation (75% less). In generations 8-16, DE slightly decreased in the 4 μm results, but slightly increased in the 2 μm results. However, generation 16 DE values of the two particle sizes only differed by 2.6%.

Fig. 10 shows the right lung original geometry with RB1, RB4, and RB10 unresolved paths for C4 and the 7-generation model of the same location. Additionally, Fig. 10 plots number of airways by generation for both models. Generations 1-3 and 7+ had the same number of airways per model. Generations 4-6 had different numbers due to the more completeness of the 7-generation model. DE was plotted in Fig. 10 (d) which corresponded to the original model and 7-generation model for 2 μm and 4 μm particles to investigate the sensitivity of deposition when the number of airways is increased. DE increased in the 7 generations model. For both particle results, differences in generations 1-3 were negligible, and differed by at most 1.5%. In the 4^{th}-6^{th} generations where number of airways were vastly different, DE was reduced in the 7-generation model results. The difference between the two results increased with particle size. At the 6^{th} generation, there was a 20% and 40% difference between the two models at 2 μm and 4

μm respectively. Beyond the 6th generation, DE was smaller than the original results, and the difference between the results increased with generation despite the numbers of airways remaining the same.

LOCAL FEATURES

Constriction in TriLLB of C4 was identified as a subject specific local structural feature. Average deposition density on the airway wall was computed and presented in Fig. 11 for 4 μm particle sizes. C4 subject exhibited significant deposition hot spot areas (10 particles/mm^2) corresponding to the local branch constriction. Deposition primarily occurred at the distal end of branches on the bifurcation walls of the child branches. Particle deposition was largest at the first bifurcation (generation 4) distal to TriLLB and deposition hot spots were prominent in the second and third bifurcations but to a lesser degree. The deposition hotspot correlated to the increase in deposition efficiency at generation 4 in Fig. 8, and the large Stk in Fig. 3. Fig. 11 (b, d, and e) presented the same branch location for HM, C2, and C3. The deposition density hotspots were not severe in the other subjects. C2 had hotspots present at the second and third bifurcations in the segmental and sub-segmental region of LB10 corresponding to the 4th and 5th generations. Deposition in the two child branches composing of the 1st bifurcation distal to TriLLB in C4 accounted for 34.1% at 2 μm and 45.2% at 4 μm of deposited particles in LLL. The same branches in C2 only accounted for 9.7% and 5.9% of total deposited particles in LLL at 2 μm and 4 μm.

Fig. 12 shows 2.5 m/s and 7.5 m/s velocity iso-surfaces for the TriLLB location for HM and C4 subjects. The constriction created a velocity jet characterized by the increase in velocity shown by the iso-surfaces. This jet was not present in the HM

subject. Average D_h^* of TriLLB is 0.229 for C4, 0.318 for C2 and 0.458 for HM subject. The Stk of TriLLB at PI in C4 was 0.098 for 4 μm particles which is 67% larger than the Stk number in C2 at the same branch.

θ_{RMB} was another local structural feature identified for analysis in Table 1. C2 and C4 had reduced θ_{RMB}. The angle shown in Fig. 2 (b) was defined as the angle between the right upper bronchus (RUB) and BrontInt created from the parent, RMB, branch. C2 and C4 subjects had reduced angles of 74.8 º and 67.9 º. Table 2 shows the θ_{RMB} for each cluster's subject. 4 μm deposition density and velocity iso-surfaces with 4 μm final deposition locations were plotted for this region and shown in Fig. 13 and Fig. 14. Similar results were present in the 2 μm case, but for simplicity were not shown.

A velocity jet was present in Fig. 14 at the distal end of RUB entering RUL for C2 and C4. Local velocities accelerated to 5+ m/s in RUB and impinged on bifurcations in the lobe of C2 and C4. This velocity acceleration did not occur until later generation branches for C3. DE of the first 3 generations of the RUL combined (generations 2-4) were calculated and presented in Table 5. At 4 μm, C4 DE was over three times greater than C2. The DE values were 4.19% and 1.24%, and at 2 μm, the DE values were 1.96% and 0.91% for C4 and C2 respectively. DE in these generations was greatest for C2 and C4 for both particle sizes. Stk in RUB (Generation 2) differed by < 1%, but in the 3rd and 4th generations, Stk of C4 was more than twice greater than C2.

Comparing DE in C3 and C4, DE in C3 was 0.82% for 2 μm and 0.90% for 4 μm particles. This equated to over 4 and 2 times less than DE in C4 for 4 μm and 2 μm respectively. C3 Stk in RUB was 3 times less than C4 for both particles sizes, and

approximately 5 times less than C4 in generations 3 and 4. C3 DE in generations 2-4 of RUL was only 10% less than C2 for 2 μm and 27% less at 4 μm.

Table 3: Total DF and $U/(M+L)_P$ DF ratio.

DF	HM	HF	C1	C2	C3	C4
1 µm						
Whole Lung	0.026	0.025	0.026	0.039	0.038	0.038
$U/(M+L)_P$	0.97	0.99	0.74	0.95	0.74	0.63
2 µm						
Whole Lung	0.028	0.027	0.028	0.043	0.040	0.042
$U/(M+L)_P$	0.96	0.96	0.75	0.94	0.75	0.62
4 µm						
Whole Lung	0.036	0.043	0.041	0.065	0.049	0.070
$U/(M+L)_P$	1.25	1.01	0.80	0.92	0.78	0.65
8 µm						
Whole Lung	0.095	0.155	0.141	0.242	0.116	0.292
$U/(M+L)_P$	1.12	1.18	1.00	0.93	0.96	0.52

Table 4: Average generational DE at multiple generation levels.

Gen.	HM	HF	C1	C2	C3	C4
2 µm						
2	0.0030	0.0032	0.0046	0.0039	0.0032	0.0056
4	0.0104	0.0126	0.0100	0.0154	0.0129	0.0207
6	0.0090	0.0105	0.0111	0.0125	0.0134	0.0132
8	0.0088	0.0137	0.0102	0.0169	0.0172	0.0209
4 µm						
2	0.0032	0.0037	0.0053	0.0044	0.0037	0.0067
4	0.0129	0.0174	0.0156	0.0211	0.0154	0.0518
6	0.0130	0.0144	0.0131	0.0218	0.0201	0.0261
8	0.0138	0.0181	0.0199	0.0219	0.0278	0.0480

Table 5: DF and DE in RUL (generations 2-4).

DF/DE	HM	C2	C3	C4
2 µm DE	0.52%	0.91%	0.82%	1.96%
2 µm DF	0.31%	0.50%	0.54%	0.67%
4 µm DE	0.61%	1.24%	0.90%	4.19%
4 µm DF	0.36%	0.67%	0.59%	1.43%

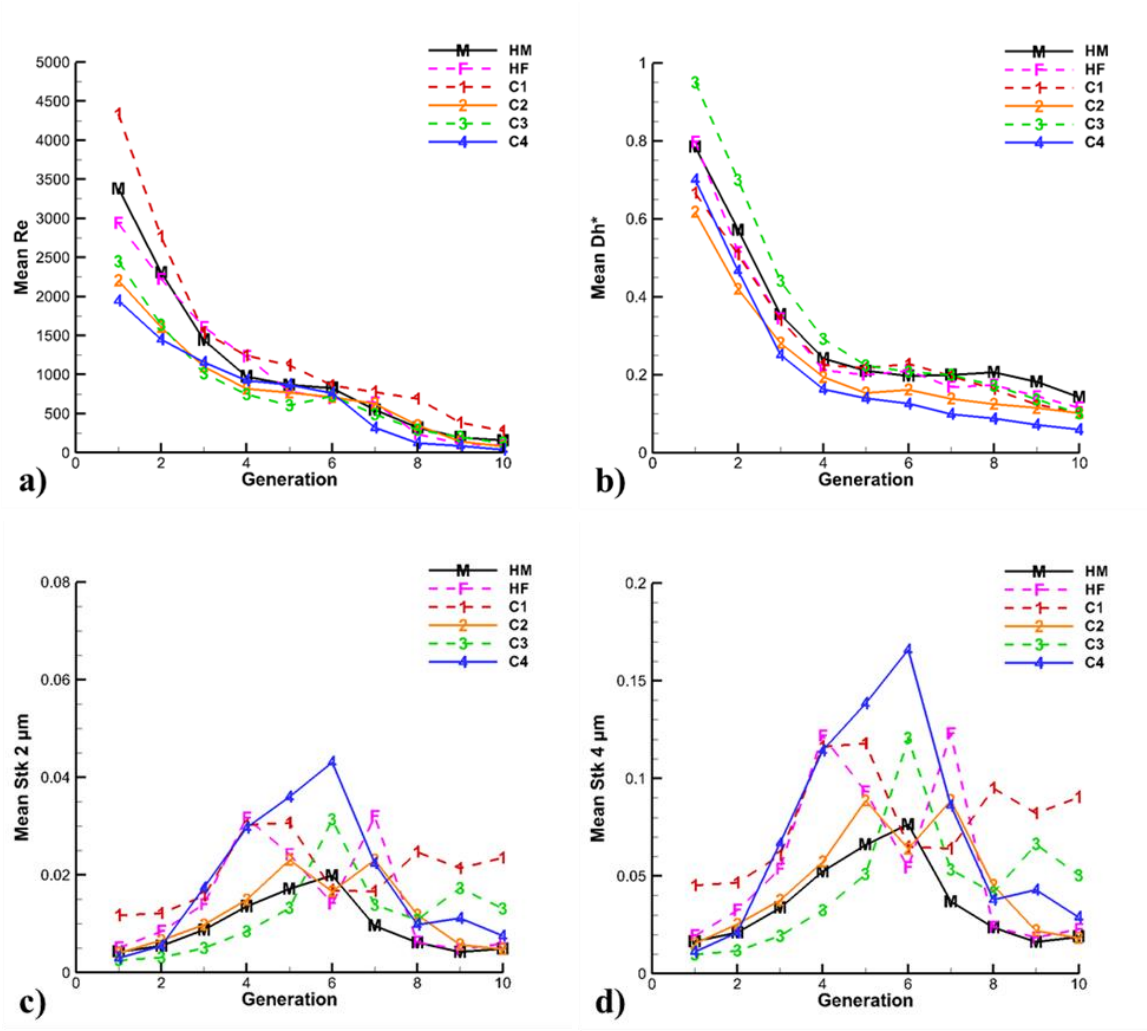

Figure 3: Generation mean of (a) Re, (b) D_h, (c) 2 µm Stk, and (d) 4 µm Stk.*

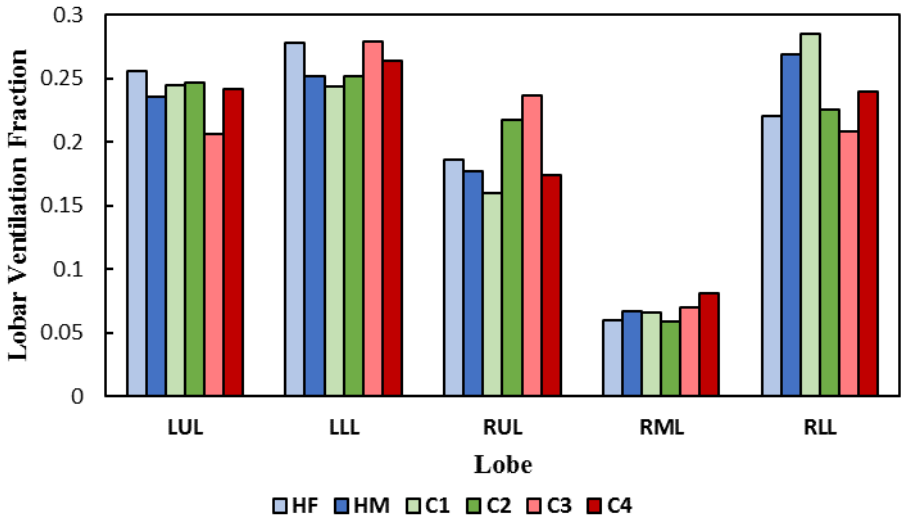

Figure 4: Regional air ventilation fractions. Blue: healthy subjects, green: non-severe subjects, and red: severe subjects. Light color shades: female subjects and dark shades: male subjects.

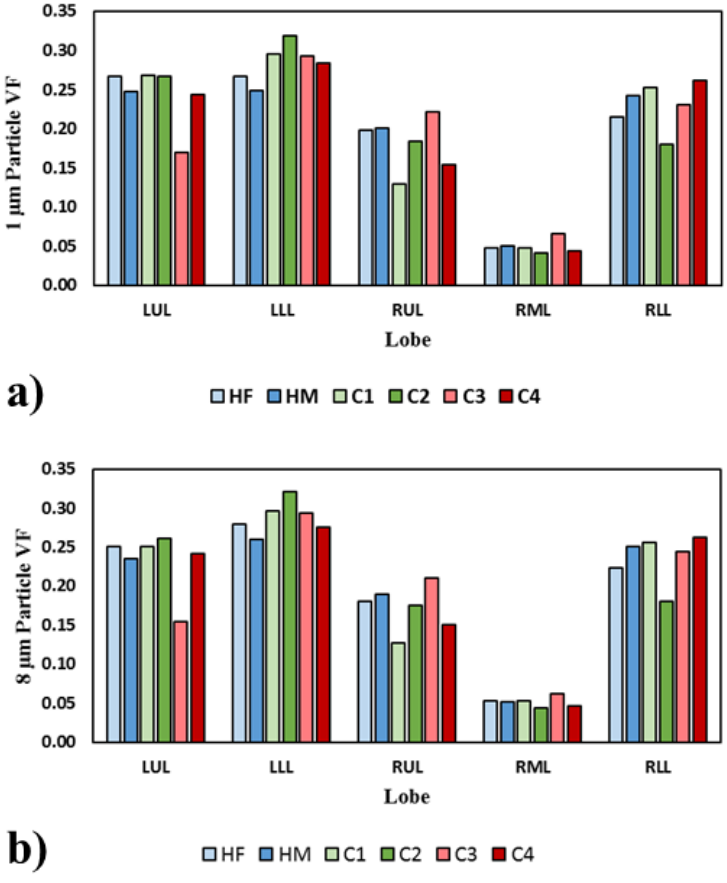

Figure 5: Regional particle ventilation fractions (VF) for (a) 1 µm particles and (b) 8 µm particles.

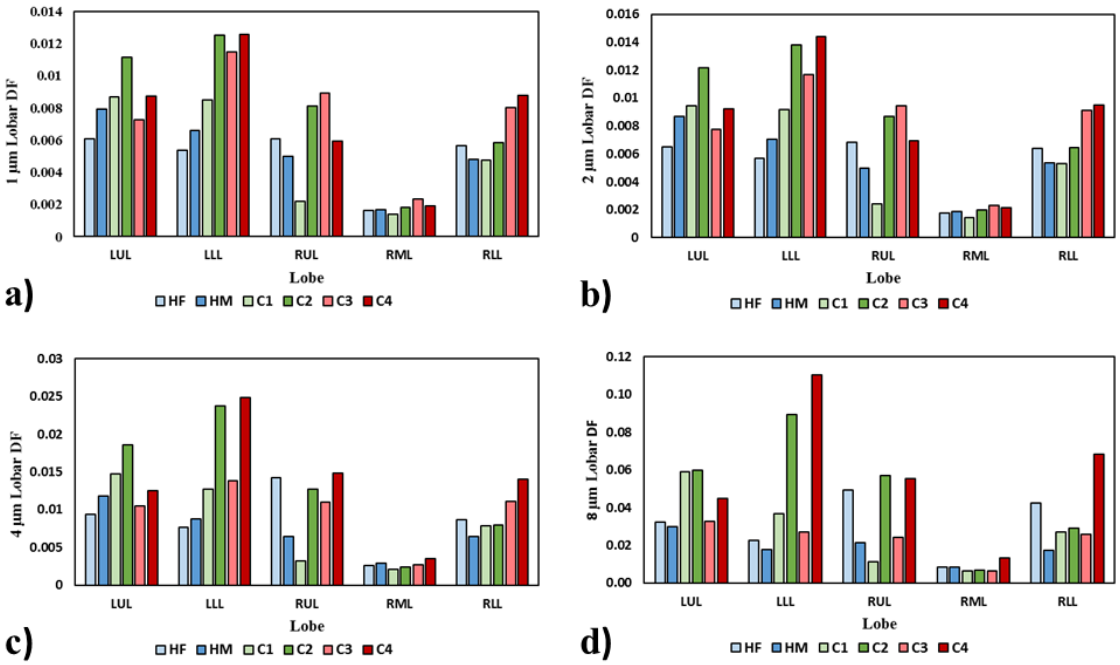

Figure 6: Regional DF for (a) 1 µm, (b) 2 µm, (c) 4 µm, and (d) 8 µm particles.

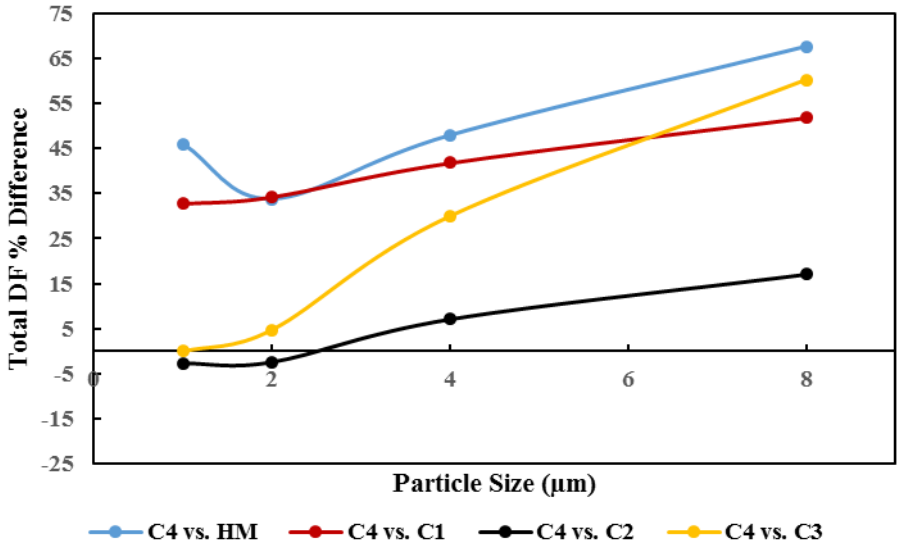

Figure 7: Percent difference in total lung DF between subjects at each particle size.

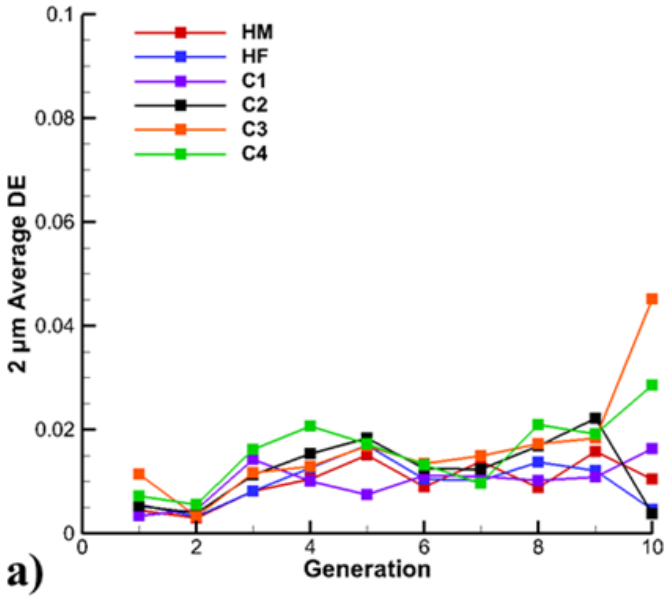

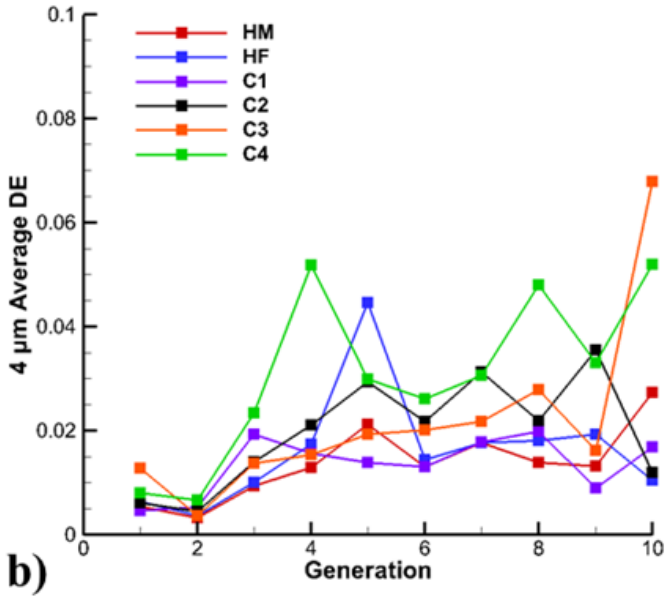

Figure 8: Average generation DE for (a) 2 µm and (b) 4 µm.

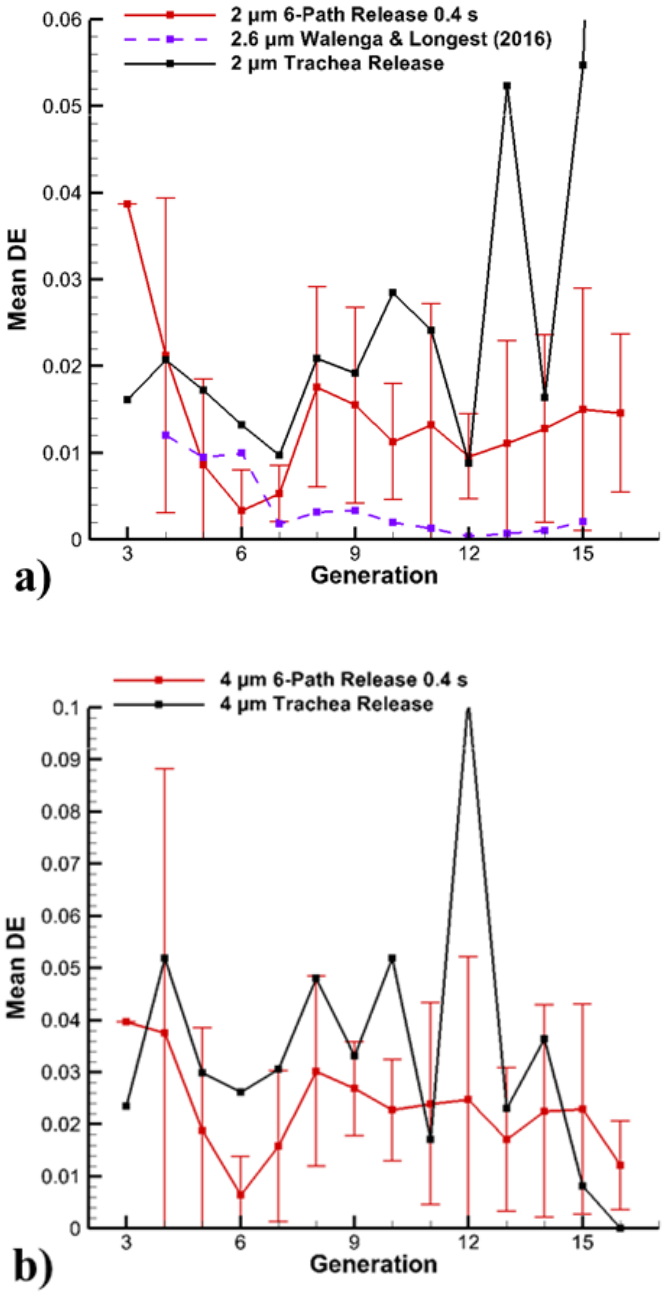

Figure 9: 6 path particle release model average DE for C4. 2 µm data compared to simulation data for 2.6 µm from Walenga & Longest (2016).

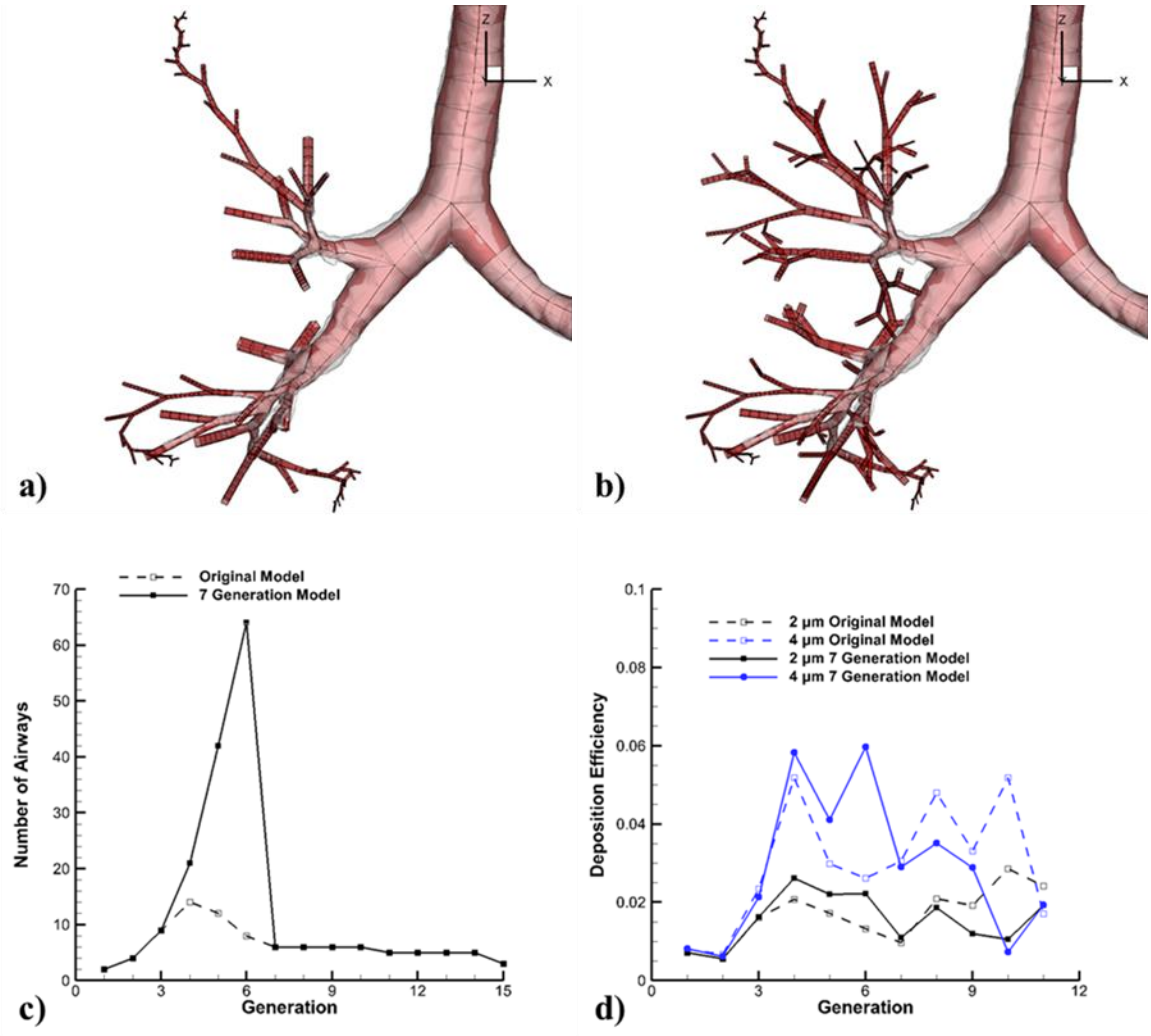

Figure 10: (a) Original C4 geometry with 6 path model with surface mesh, (b) C4 complete airway through 7 generations model with surface mesh, (c) number of airways by generation for both models, and (d) DE for both models.

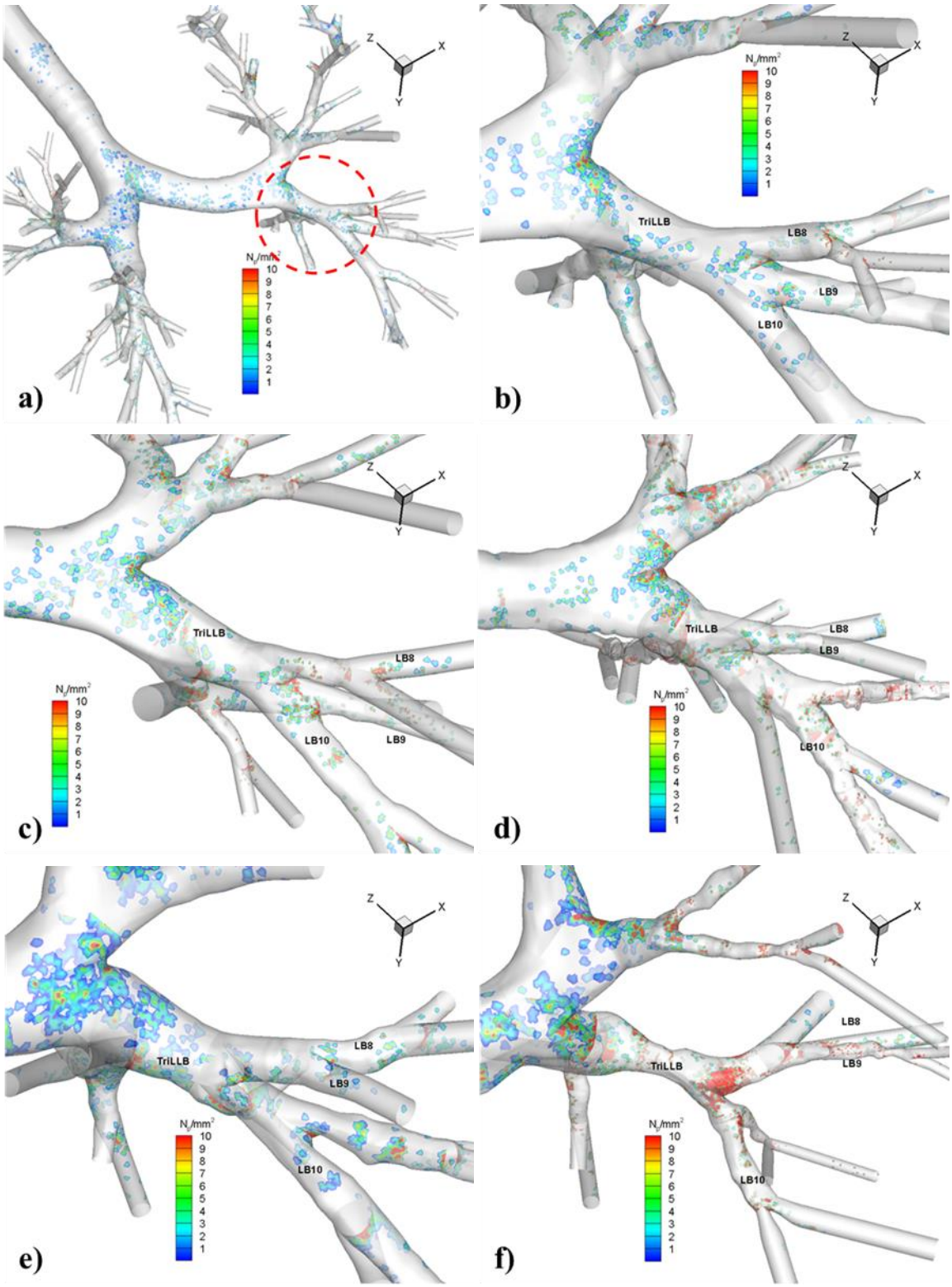

Figure 11: Average DD plots of TriLLB for a) HM full lung location reference, b) HM, c) HF, d) C2, c) C3, and d) C4. DD presented as number of particles per mm^2. Plots associated with 4 μm particle simulations.

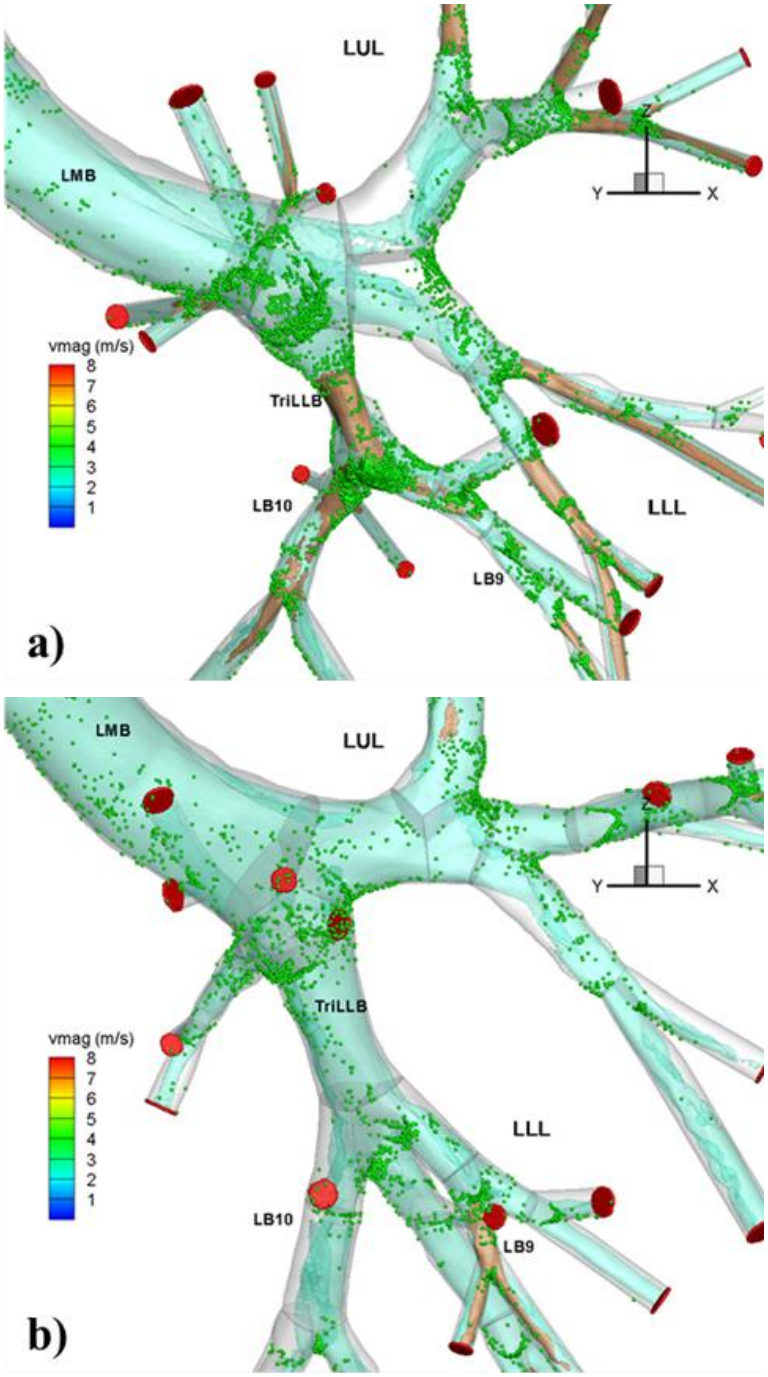

Figure 12: 2.5 m/s and 7.5 m/s velocity iso-surfaces of the LLL of (a) C4 and (b) HM with final particle locations. Green particles are deposited and red particles exited the domain.

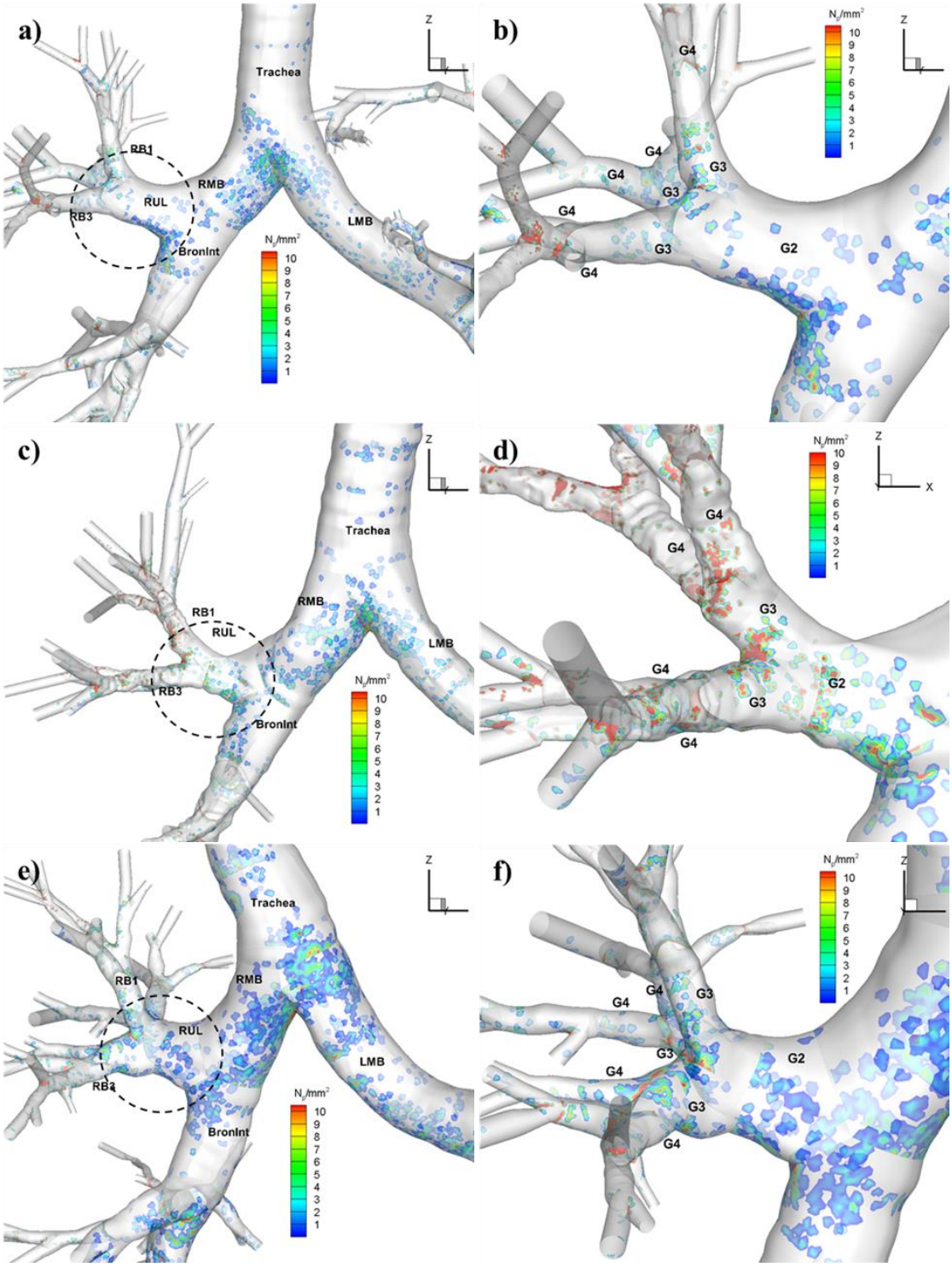

Figure 13: Average DD in the RUL of (a, b) HM, (c, d) C2, (e, f) C3, and (g, h) C4 for 4 μm particles. Circle in the figures in the left column highlights the region zoomed into in the right column figures. Branches and generation numbers are labeled.

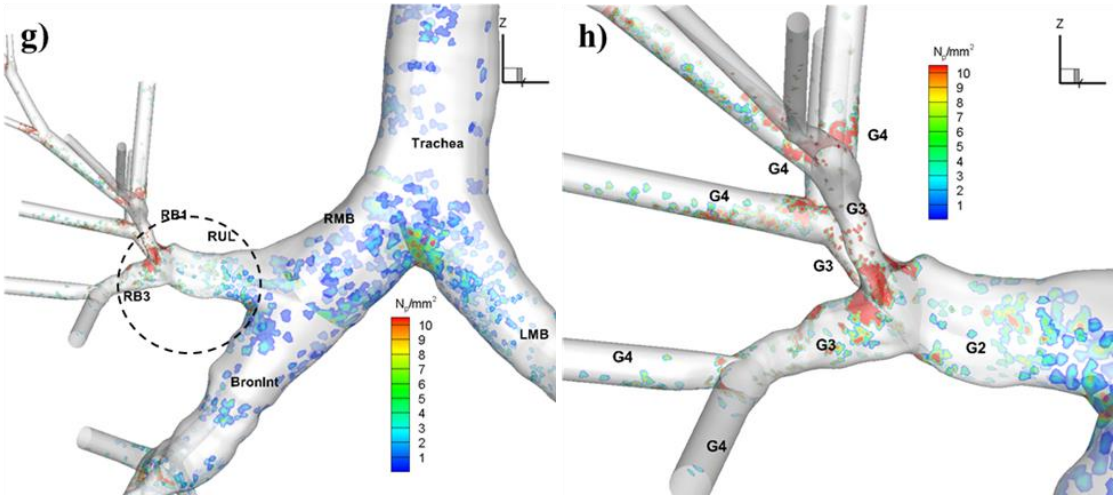

Figure 14: Continued

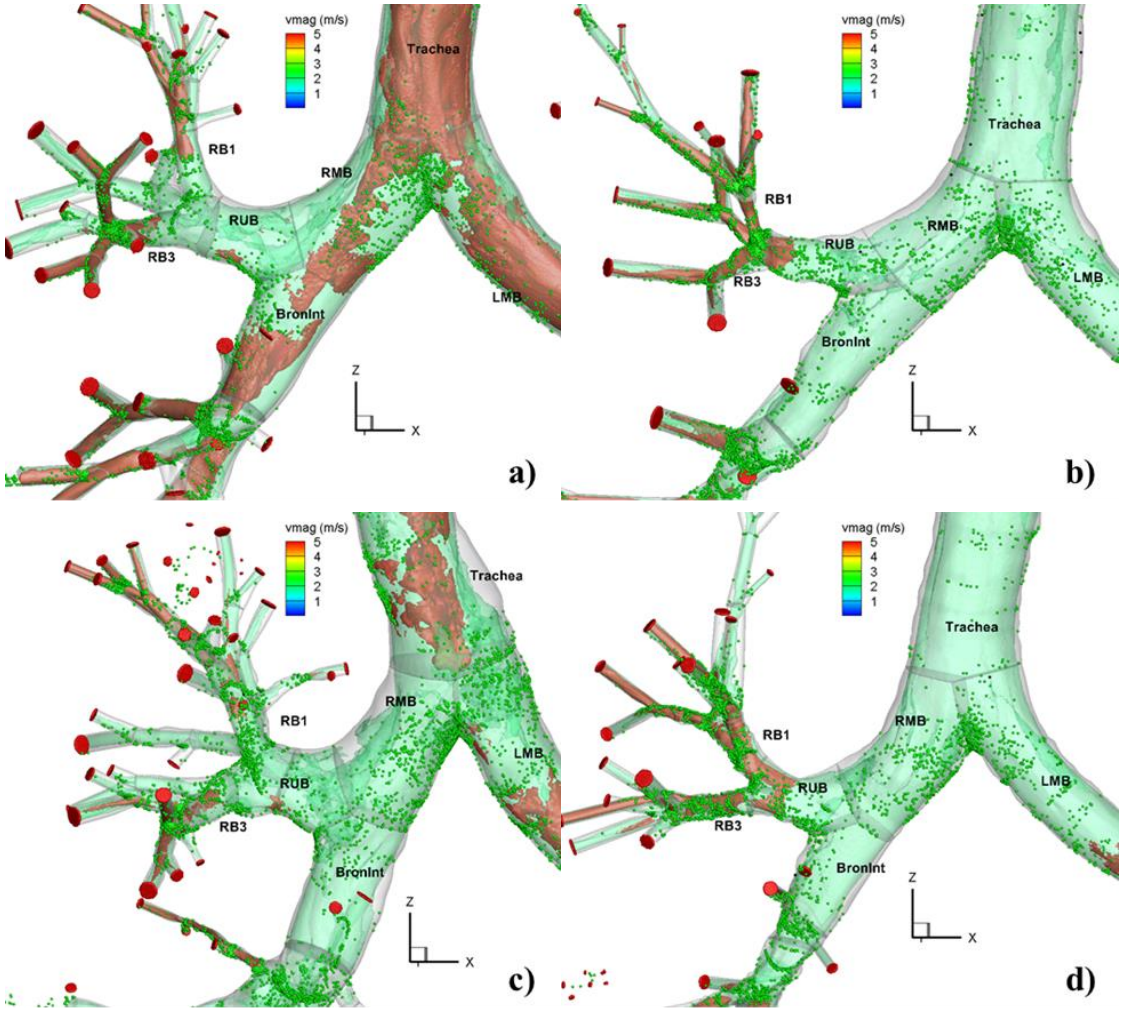

Figure 14: 4 μm particle simulation velocity iso-surface plots of 2 m/s (green) and 5 m/s (red) in a) HM, b) C2, c) C3, and d) C4 with branch labels.

DISCUSSION

The aim of this study was to utilize a cluster-based approach in conjunction with multiscale high-fidelity LES CFD lung simulation methods to assess the effects of cluster image variables on fluid transport, particle transport and deposition. For this aim four imaging-based features of AirT%, $\theta_{RMB,}$ D_h^*, and Jacobian were selected as characteristics likely to influence particle transport and deposition patterns. Particle transport results between clusters was compared through analysis of particle ventilation, DF, DD, and DE along with CFD simulations. This was a novel study because the knowledge of inter-cluster variability in particle transport could potentially help improve inhalation drug delivery in asthma sub-populations.

One of the most interesting observations from this study was the common lung function characteristics between C2, C3, and C4 and the differences in particle deposition. DE was largest in subjects characterized by airway constriction and not those classified by asthma severity. DD was prominent in locations of local constrictions in the segmental airways, concentrating deposition on bifurcation walls distal to constrictions due to the impaction of constriction-induced jet flow. Total DF was also largest in constricted airway subjects, but regionally this was not always the case for all lobes due to particle ventilation differences. The deposition differences between the constricted subjects and non-constricted subjects was exacerbated as particle size increased. This observation suggested that structural characteristics, specifically airway narrowing, had a more profound effect than functional characteristics on deposition statistics at larger particle sizes (>2 μm). Martonen et al. (2003) made the same observation when predicting particle deposition by generation in asthmatic lungs with different degree of

constriction. In their study, they applied heterogeneous constriction to various generations in an idealized mathematical lung model geometry and found deposition increased in constricted generations. Walenga & Longest (2016) simulated steady flow particle transport in constricted airways using a homogenous constriction model on an airway geometry with complete airway through 3 generations, and stochastic individual path models to evaluate deposition in small airways similar to this study. Their results concluded that low amounts of particles deposit (<1%) in small airways. Their results were more consistent and had less variations. The differences could be explained by DE uncertainty mentioned in Miyawaki et al. (2016), their idealized geometric model and homogenous constriction, and unrealistic symmetric flow distribution beyond central airways.

The combination of the 6 major paths, and multi-stage particle release at the segmental airways of the 6 paths showed promise for efficiently improving deposition statistic strength at small airways. The DE results were greater than Walenga & Longest. (2016) data in generations 8-15, however the geometric model and boundary conditions in this study were more realistic, and the progression of DE in generations 8-15, mirrored Walenga & Longest (2016), only translated higher. The generation-to-generation variability of DE decreased in the multi-stage release results at the higher generations compared to the original results and is evidence of improvement. The 6-path multi-stage release method would reduce computational costs and feasibility. To achieve the same results as the 6-path segmental airway release location data by releasing particles at the trachea would require the number of particles released to be increased by a factor of

approximately 100 if one assumed that each bifurcation resulted in half the particles entering each child branch.

Local structural features showed to be integral in particle deposition and local flow characteristics, and dominated regional deposition patterns through inertial effects. While overall constriction lead to an increase in particle deposition compared to non-constricted subjects, the large increases in deposition efficiency seen for C2 and C4 at the 4^{th} and 5^{th} generations were caused by local constrictions such as the TriLLB constriction in C4.

The influence of local constrictions is prevalent to discussion on Stk and its governing on particle dispersion in turbulent flow. It is well researched that Stk characterizes how particles will travel in a fluid. Particles with low Stk ($\ll 1$) will follow the fluid streamlines and act as a mixture. Particles with large Stk ($\gg 1$) have little dispersion and are largely unaffected by fluid deflections. These particles mostly deposit from inertial effects and do not follow streamlines when fluid transport direction is altered. Particles with Stk approximately 1 will migrate to the edges of turbulent eddies (Crowe et al. 1985, 1988). The TriLLB constriction in C4 was so significant that branch diameter decreases by approximately 55% in the middle of the branch where the constriction happens. This constriction resulted in an average Stk at PI that was approximately 4 times greater than C3 and 3 times greater than C2 according to Fig. 3. While average Stk values were not greater than 1, the structural variable results suggested the influence of increased Stk on inertial deposition by impaction in C4 and other constricted airways. C2 average generational Stk values were not exclusively larger like C4. Despite this, deposition patterns were larger, especially in the 4 μm particle results.

This raises the concern on if Stk is the most appropriate dimensional analysis term for characterizing deposition. Lower average Stk values in C2 corresponding to larger DE and DF values could be the result of local constrictions that are more extreme being averaged out.

The decreased RMB branching angle that is common in C2 and C4 is also an important local feature for drug delivery considerations. Fig. 13 and Fig. 14 showed increased DD at bifurcations distal to RUL that correlated to a velocity jet forming similar to TriLLB in C4. Compared to C3, DE was more than 10% and 25% larger in C2 and C4 for 2 μm and 4 μm respectively. However, the degree of effect that the reduced angle had on deposition was unclear, because in addition to the reduced branching angles, C2 and C4 also had local constrictions present at the RUB which could be the reason for the formation of the velocity jet towards the end of RUL. As mentioned previously in the results, DE was increased in generations 2-4 of RUL in C2 and C4 compared to C3. The normalized RUB branch diameters were 0.32 and 0.31 for C2 and C4 subjects which was approximately two times smaller than the healthy subject, and C3 (0.60 and 0.61). The presence of the diameter constriction, and the DF and DE results would indicate that constriction was more prevalent for deposition due to its global presence. The significance of the branching angle on deposition compared to the decreased diameter of RUB requires further investigation using control subjects that contained one of the local features (reduced branching angle or RUL constriction) without the other. It is possible that the reduced angle was more influential on particle ventilation and DF rather than DE. According to Fig. 5, HM and C3 had a higher particle ventilation in RUL. For 2 μm results, approximately 2% and 30% more particles entered RUL of HM compared to C2

and C4 respectively. For C3, the percentages were approximately 11% and 30% more particles ventilated to RUL. This was a significant finding for consideration of drug delivery. Higher DE did not always correlate to higher DF. For example, for 2 μm, DF in RUL for C3 was larger than C2 and C4 largely due to more particles entering the lobe. If the targeted drug location were in the RUL, a higher dosage would be necessary for subjects in C2 and C4 to be effectively treated.

The local subject specific features highlight the need for imaging-based multiscale CFD methods to obtain the most accurate physiologically realistic analysis of particle transport in diseased lungs. Mathematical models such as the symmetric Weibel (Weibel, 1963) and asymmetric Horsfield (Horsfield et al. 1971; Khorasanizade et al. 2011) models without further modification can only provide a simplified non-subject specific straight tube based geometry. Many researchers have applied an airway cast model by Yeh & Shum (1980) in conjunction with a physiologically realistic bifurcation model (Heistracher & Hofmann, 1995) to create asymmetric airway models with physiological realistic airway branch lengths, average diameters, and bifurcations (Longest et al., 2012; Tian et al., 2010; Walenga & Longest., 2016). This method still fails to capture local and structure variations. Obtaining subjects, with characteristics specific to the aim of your study, to create casts is not practical, thus imaging-based geometries is the best solution. While image resolution limits anatomically precise generations, techniques such as the volume filling method used in this study provide a method to create accurate airway geometries to terminal bronchioles (Miyawaki et al., 2016; Tawhai et al., 2004).

From a drug delivery perspective, the deposition results between clusters provide valuable insight for research associated with improving drug delivery from dosimetry

perspective. Choi et al. (2017) suggested from their clustering membership that due to the differentiable characteristics of C3 and C4 subjects, it might be beneficial to group by independent phenotypes. The DE results supports this suggestion. One of the defining characteristics of C3 was wall thickening which may be caused by inflammation and is typically treated with an inhaled cortical steroid (ICS). From Choi et al. (2017) it was reported that 76% of patients grouped in C3 used high dosage ICS, and C3 was also associated with blood lymphopenia due to the high dose ICS. It is of question whether the high dose ICS is effective to the airway wall inflammation of entire lungs. For instance, the low DE in C3 would suggest that increasing ICS dosage with small size may not be effective for improving inflammation reduction at the levels of segmental airways, whereas it may be effective to the inflammation of peripheral airways. On the other hand, an increase of the particle size however would increase Stk and be a cause for more inertial deposition and possibly more efficient inflammation reduction. This information may be referred to determining cluster-specific drug size between clusters to improve deposition of targeted regions.

On the other hand, C2 and C4 were characterized by airway narrowing and had increased deposition in segmental airways that was exacerbated at larger particle sizes (4 μm) (Fig. 8), more significantly in C4. Bronchodilators were a common treatment for airway narrowing. Effectively treating airway narrowing would require high drug penetration past the segmental and sub-segmental airways, which could be achieved with smaller particle sizes. Smaller particle sizes however may overshoot the desired location, which is why many researchers have suggested using dynamically sized particles and growing particles to a size that would deposit in a specific location (Asgharian, 2004;

Ferron et al., 1988; Longest et al., 2011; Son et al., 2013; Winkler-Heil et al, 2014). The link between the starting particle size and rate of growth associated desired location has not been concretely specified. Using the DE information in Fig. 8 and Fig. 9 with statistical analysis of the time required for particles to reach the segmental airways could provide insight on where airway constriction is most adverse on deposition, and provide information for determining initial particle size of an inhaled drug needed to penetrate effectively past high DE constrictions. If particles could remain smaller than 4 μm until generation 6-7, deposition might increase significantly in small airways.

Deposition statistics contain an element of uncertainty. When interpreting the deposition results, it is important to remember that CT-image based CFD simulations can have up to 7% uncertainty in deposition results compared to more accurate 4DCT-image based CFD simulations (Miyawaki et al. 2016). The 7% uncertainty is not large enough though to conclude that C2 and C4 increased deposition is a product of uncertainty. An additional source of uncertainty is from CT resolution limitations. CT resolution dictates the number of CT-resolved branches available for geometry construction, and computational costs limit the number of unresolved branches that can be attached to extend geometries. In a perfect scenario, the entire lungs are modeled with all paths to terminal bronchioles existing. Additionally, in the current model, ending branches must be excluded from analysis to avoid a boundary condition effect from the prescribed outflow condition. A relationship between deposition results and the number of available airways exists. To mitigate the issue of ending branches, the complete 7-generation model for C4 was created and investigated for sensitivity analysis. Deposition efficiency results increased in the 7-generation model at generations (4-6), where complete airways

now existed, further supporting the theory that constriction is most influential on deposition in segmental and sub-segmental (generations 3-6) airways. Despite the number of airways for deposition statistic calculation remaining the same in generations 7-15, DE decreased compared to the original model results. This is associated with a lack of particles released for the number of airways present. More airways equate to more paths for particles to follow, and more particles are required to be released to obtain results that are no longer sensitive to numbers of particles. To combat this issue, we applied the particle tracking method where particles were released at the segmental airways leading to each of the 6 paths. A mathematical relationship of the number of particles necessary for statistically strong results given the desired number of complete airway generations would be a big step in improving research efficiency.

Definitive conclusions on gender comparison with associated clusters were not able to be made due to both subjects selected with constricted airways being male. Future studies can make use of these findings and apply them to a larger sample size per cluster, or female subjects from cluster that are not gender biased and study the MICA feature differences between genders. Additionally, future work can emphasize the relation between lung structural and functional imaging features and small airways using a whole lung or lobe model with complete air trees to terminal bronchioles.

CONCLUSIONS

The current study demonstrated how the recently proposed important regional airway features from multiscale imaging based cluster analysis of asthma patients govern regional and local airflow and particle transport during deep inhalation in association with global lung features and highlight extensive subject variability across clusters.

Regional and generational DE and DF values were predicted using CFD simulations for an inspiration profile corresponding to application of MDI inhalers. Airway luminal narrowing in C2 and C4 contributes to deposition statistics in lobar, segmental, and in some instances sub-segmental airways. AirT%, in C4, has definitive lung functional effects through reduction of FRC and IC, but the correlation to particle deposition has not been determined yet and requires future work. Luminal airway narrowing contributes the most to deposition patterns.

The findings convince the importance of understanding the MICA features of structure and functions in assessing efficacy of inhaled drug delivery in asthma patients and highlights the importance of utilizing MICA feature for pharmaceutical drug and drug delivery selection, rather than asthma severity. Despite their common severe asthma classification, subjects in C3 and C4 have very different characteristics and deposition patterns. The same drug and drug delivery method applied to both clusters will have profound differences, whereas subjects in C2 would benefit more of drug developed for C4 subjects. Regional airway constriction and AirT% features limit ventilation and deposition of particles beyond segmental airways for particles greater than 2 μm, further stressing the need for continued research on dynamically sized particles through hygroscopic growth for effective treatment for asthmatic subjects with airway constriction.

CHAPTER 2: HYGROSCOPIC GROWTH MODEL VALIDATION

INTRODUCTION

When discussing pharmaceutical drug delivery in the human lungs, one topic that is frequently brought up is hygroscopic growth. It is well documented and mentioned previously that inspired hygroscopic particles, such as sodium chloride, when exposed to the environmental conditions inside the human respiratory track will act as nuclei for droplets to form (Friedlander et al. 1994; Hinds 1999). Through the process of deliquescence and continual vapor diffusion, droplets grow until they reach a steady state size. This particle growth plays an important role on deposition in the lungs. With a small initial diameter, the particle can penetrate the oropharyngeal airway and enter the lungs where droplet condensation on the particle will increase the diameter and lead to lung deposition and retention.

There are two main methods for applying hygroscopic growth to aerosolized drug delivery that are being investigated. Enhanced condensational growth (ECG), involves delivery of a sub-micron particle with super saturated air greater than body temperature. The supersaturated air cools causing condensation onto the drug droplets (Longest et al., 2010). The second method, enhanced excipient growth (EEG), involves manufacturing drugs such that the aerosol sprayed is composed of a combination of hygroscopic excipient and drug. The hygroscopic excipient stimulates the particle growth in the lungs (Longest & Hindle, 2011).

Longest et al. (2010) attempted to characterize ECG using *in vitro* measurements and numerical predictions. In their study, they combined nano-aerosols with saturated and supersaturated water vapor and injected it into a tube that had dimensions like that of the average human trachea. Measurements were taken for three particle sizes at three

humidified air stream temperatures. In all instances, aerosol growth was measured and the degree of growth increased with inlet temperature. Growth ratios between final diameter and initial diameter ranged between 1.5 and 8 depending on the conditions. The largest rate of increase occurred between 25 °C and 30 °C. Only a small difference in final size was recorded between 30 °C and 39 °C. For example, from 25 °C to 30 °C, the 560 nm particle final diameter increased from 610 nm to 2256 nm compared to 2664 nm from 30 °C to 39 °C. The study concluded that enhanced condensational growth can increase lung retention of drugs, reduced drug deposition in the mouth, and more efficient drug delivery to targeted regions or lung generations. In a follow up study, the same group compared the *in vitro* results above with CFD results of the same experiment. The geometry, boundary conditions, and particle sizes were all consistent. CFD simulations were done with-one way and two-way coupling between the water and air. The group concluded that when two-way coupling was included, growth results showed agreement to the *in vitro* data and indicated that the separate inlet humid air stream temperature and two-way coupling greatly impacted the final aerosol size. They concluded that ECG could be an effective method for growing hygroscopic particles above 2 μm, and increasing lung retention (Longest and Hindle, 2010). Tian et al. (2010) further demonstrated that the ECG is an effective method for delivering aerosolized drugs to the lungs by using CFD to model a single path from the oral cavity to the end of the tracheobronchial region down to the 15^{th} airway generation. Airway cast measurements were used to create the geometry. Negligible deposition occurred in the mouth throat region and tracheobronchial deposition rates were between 32% and 46%. ECG has also been shown as a viable method for improving drug delivery in non-invasive nasal ventilation with constant flow

conditions. In another *in vitro* study, ECG applied to nasal drug administration showed drug deposition fractions decreased from 72% to 14% in the nose, mouth, and throat region. Further CFD analysis concluded that by extrathoracic deposition could be further reduced by increasing the saturated air stream to body temperature (Longest et al. 2011).

The second method of controlled particle growth, EEG, is versatile and works well for drugs that are naturally hygroscopic or hydrophobic. Longest & Hindle (2011), tested a variety of 50/50 drug and excipient combinations and could observe growth ratios ranging from 1.6-2.9 from *in vitro* experiments that were validated with CFD models. In another study, Son et al. (2013) investigated developing a combination drug and excipient powder for EEG in DPI inhalers. Using an *in vitro* model of a realistic mouth-throat model, they observed only 4.1% deposition in the model using their developed dry powder. Both methods appear to be effective at increasing deposition in the lower tracheobronchial regions, however EEG seems to be the more practical and simpler method for application into wide spread personal pulmonary drug delivery use.

Numerous numerical models have been developed to characterize hygroscopic growth of particles with the goal of implementation in CFD models (Asgharian, 2004; Broday & Georgopoulos, 2001; Ferron et al., 1988; Longest & Hindle, 2010; Winkler-Heil et al., 2014). Understanding the physics and chemistry that govern the growth of hygroscopic particles is not trivial and still being researched.

Each researcher has their own variation applied to their growth model used. The foundation for all the models typically starts with Maxwell's differential equations for vapor diffusion on a salt-water droplet, where the driving force of growth is the partial vapor pressure gradient that exists between ambient surroundings and the droplet. From

there, researchers have modified the base equation to come up with their own growth models. For example, Broday & Georgopoulos (2001) suggested that a change in droplet diameter is coupled with a change in droplet temperature, and that they must be iteratively solved simultaneously. This is similar to Ferron (1977) who suggests droplet diameter is coupled with heat transport into the droplet. Winkler-Heil et al. (2014) and Ferron (1977) apply Raoult's Law to correct the partial vapor pressure for the presence of salt creating a dilute solution and reducing equilibrium vapor pressure. Raoult's law establishes that the individual component vapor pressures of a mixture are defined as the multiplication of the mole fraction and vapor pressure of each component. Winkler-Heil et al., applied their growth model to a stochastic lung model and evaluated deposition fraction of various salts on a generational level. Their depositional data showed good agreement when considering inter-subject variability and modeling assumptions and their growth data suggested a growth factor ranging from 1.75-5.33 depending on salt type, initial diameter size, inspiration, or expiation.

Another method for accounting for changes in mixture vapor pressure due to the presence of salt is through implementation of a quality of a solution referred to as water activity (Broday & Georgopoulos, 2001; Asgharian, 2004). Water activity is a term that has been made popular through food sciences as a method for quantifying the quality of food and ability for microorganisms to grow on them. A simplified definition of water activity is the ratio of partial vapor pressure of a solution to the partial vapor pressure of the pure liquid at the same temperature (Barbosa-Cánovas et al., 2008). In essence, droplet growth is stimulated by the difference between water activity and ambient RH.

Asgharian (2004) was able to implement his growth model that includes water activity simplification into an existing numerical model for fluid and particle transport in lungs. His model predictions showed agreement with available experimental data and it was concluded that most submicron particles deposited between the 15^{th} and 20^{th} generation. Time required to reach an equilibrium size was proportional to initial particle size, and submicron particles attained equilibrium sizes in less than 1 second.

Many attempts have been made at validating growth models. The default setup that researchers typically utilize is that of a humidified tandem differential mobility analyzer (HTDMA), or sometimes called a dual differential mobility analyzer (DDMA), where one DMA is used to generate a mono-disperse aerosol, and the second is used in combination with a condensation particle counter (CPC) to measure final diameter of particles as they turn into droplets (Biskos et al., 2006 & Li et al., 1992). HTDMA setups have become common in experimental measurements largely because of their high resolution compared to other measurement devices and accuracy within 2%. Measurement is achieved by applying a charge to particles. Different sized particles acquire different charges, and based on the scanning voltage size channel and flowrate, particles in a narrow diameter bin size are filtered out and counted. These systems can measure particles between 3-1000 nm based on flow conditions (McMurry, 2000). HTDMA setups are popular in atmospheric science where the rate of change of a particle is not as important, there are not flow constraints, and the particles of interest are less than 100 nm. Biskos et al. (2006) measured growth factors, ratio of grown diameter to original diameter, of atmospheric particles with initial diameters ranging from 6-60 nm at different humidity levels. They determined that growth is negligible until around 80%

relative humidity. Li et al. (1992) measured final growth of particles with initial diameters of 10-200 nm at 99% relative humidity and 37 °C and 22 °C. They plotted there results against model results with good agreement. When evaluating growth with respect to the respiratory system, this method is not ideal. Flowrates associated with inhalation patterns decrease the range of particles the DMA is able to measure, and this system is unable to capture any transient effects of growth due to long travel times within the DMA and CPC before being measured.

Longest et al. (2010) addressed measuring hygroscopic growth and validating their growth model from a different direction. Their group used an Anderson Cascade Impactor (ACI) to measure final size. An impactor functions as a series of stages that correlate to diameter size bins. As an aerosol stream is directed into an impactor, particles get caught on the stage due to inertial effects. Each subsequent stage has a lower limit of sized particles that can pass through. Afterwards, stages are measured and particle counts are back calculated based on mass. This method allows for measurement of particles in the micrometer range, measurement of transient nature of growth, and uncertainty associated with humidification, or dehumidification from the DMA is eliminated. The drawbacks of this method mainly are associated with the resolution of size measurement. In their experiment, the percent difference in measured growth and computer modeled growth ranged from 5% - 82%. It was not mentioned how many stages the impactor had, but typical impactors have 8 stages ranging from 400 nm to 10 micrometers. This size resolution was most likely the main contributor towards their error. For lung application, an optical particle counter appears to be the best method for measurement.

With variations in growth models and complex thermodynamics and physics associated with them, interpretations of previously mentioned models is not trivial. It is evident an in-depth analysis of model components that highlights key components is necessary for future researchers and collaborations. The model proposed by Broday & Georgopoulos (2001) appears to be the most complete and thoroughly explained. Even with the explanation, comprehension is difficult. It is the aim of this paper to present their model for growth of a salt particle in such a way that allows for easier implementation in future research by explanation of unclear terms and simplification. Additionally, this paper aims at replicating experimental hygroscopic growth measurements through an alternative measuring approach and validating the previously mentioned numerical growth model.

METHODS

HYGROSCOPIC GROWTH (NUMERICAL METHODS)

The growth model selected for adaptation into this research was the Broday & Georgopoulos (2001) model. Of the various models studied, this one appeared the most complete and is one of few that solves directly for droplet diameter rather than droplet mass. The model was based on solving a system of coupled differential equations for growth of a salt particle. The two equations were change in droplet diameter due to mass diffusion, and change in droplet temperature due to dissipation of latent heat of evaporation. The two equations in their final form are presented below.

$$\phi \frac{d\phi}{dt} = \frac{4D_v^* M_w p^S(T_a)}{R\rho_d}\left[\frac{RH}{T_a} - \frac{a_d}{T_d}\right] \tag{10}$$

$$\frac{dT_d}{dT} = \frac{3}{\phi^2 c_{p,w}}\left[\frac{4k_v^*}{p_d}(T_a - T_d) + h_{fg}\phi\frac{d\phi}{dt}\right] \tag{11}$$

The nomenclature for these equations and subsequent discussion can be found in the corresponding chapter's appendix. The arrival of the final form of the equation presented above came from making substitutions including the Clausias-Clapeyron effect, Kelvin effect, diffusivity, thermal conductivity, and water activity constant for determining the partial vapor pressure in space far from the droplet.

The Clausias-Clapeyron (12) effect describes the saturation vapor pressure being dependent on ambient temperature and the droplet temperature. Therefore, the droplet temperature became a function of the ambient temperature. The Kelvin Effect (13) is a process where spherical droplets exert a higher vapor pressure then non-spherical surfaces.

$$p^s(T_d) = p^s(T_a)exp\left\{\frac{h_{fg}M_w}{R}\left(\frac{1}{T_a}-\frac{1}{T_d}\right)\right\} \quad (12)$$

$$p_d^S = p^s(T_d)exp\left\{\frac{4M_w\sigma}{R\rho_w\phi T_d}\right\} \quad (13)$$

There is also a "Solute Effect" due to solutes having lower vapor pressure than pure water. Because the Solute Effect has a greater influence than the Kelvin Effect, salt droplets can grow in conditions less than supersaturated. Water activity is used to define the Solute Effect. As mentioned previously, water activity is the ratio of vapor pressure of a mixture to the vapor pressure of a pure substance at a reference temperature. In this case, it is the ratio of salt water solution vapor pressure to pure water vapor pressure at the same temperature. By defining water activity of a "flat" solution as a_w, the water activity of a salt water droplet a_d (14) can be approximated by combining a_w with the Clausias-Clapeyron effect and the Kelvin effect. Values for water activity of a "flat" solution were determined empirically through fitting a quadratic equation to data from

Kitic et al. (1986) as a function of mass ratio of salt in the droplet. That equation can be found in the material properties tables.

$$a_d = a_w exp\left\{\frac{4M_w\sigma}{R\rho_w\phi T_d} + \frac{h_{fg}M_w}{R}\left(\frac{1}{T_a} - \frac{1}{T_d}\right)\right\} \quad (14)$$

Lastly, modified diffusivity (15) and modified thermal conductivity (16) were substitutions made to account for differences in operating between the continuum and molecular regimes.

$$D_v^* = D_v\left[\frac{1}{1+2\delta_c\lambda/\phi} + \frac{2D_v}{\phi\alpha_c\sqrt{RT_d/2\pi M_w}}\right]^{-1} \quad (15)$$

$$k_v^* = k_v\left[\frac{1}{1+2\delta_c\lambda/\phi} + \frac{2k_v}{\phi\alpha_t\rho_a c_p\sqrt{RT_a/2\pi M_a}}\right]^{-1} \quad (16)$$

Comprehension of these equations can be quite cumbersome, especially when considering spatial variance of temperature and humidity, causing variables to become functions of temperature and humidity.

Managing these equations becomes simpler through grouping of terms into constants. For validation of the model against our *in vitro* experiment, constant temperature and RH are employed to mirror the experiment. In real application to lung modeling this would not hold true due to temperature and vapor gradients in the respiratory track. This method reduced the complexity of the equation. Through this method, 14 constant groups were identified. Table 6 displays these constants. One important modification made to the model involved using the thermal conductivity and specific heat ($c_{p,m}$) of a vapor-air mixture (k_v), as presented by Tsilingiris (2008). Substituting these constants into equations (10, 11, 14, 15, and 16) yielded the following simplified equations (17-21).

$$k_v^* = C_1\left[\frac{1}{1+C_2/\phi} + \frac{C_3}{\phi}\right]^{-1} \quad (17)$$

$$D_v^* = C_4\left[\frac{1}{1+C_2/\phi}+\frac{C_5}{\phi}\right]^{-1} \quad (18)$$

$$a_d = a_w exp\left\{\frac{C_8}{\phi T_d}+C_9\left(C_{10}-\frac{1}{T_d}\right)\right\} \quad (19)$$

$$\frac{d\phi}{dt} = \frac{C_6 \boldsymbol{D_v^*}}{\phi \boldsymbol{\rho_d}}\left[C_7-\frac{\boldsymbol{a_d}}{T_d}\right] \quad (20)$$

$$\frac{dT}{dt} = \frac{C_{11}}{\phi^2}\left[\frac{C_{12}\boldsymbol{k_v^*}}{\boldsymbol{\rho_d}}(C_{13}-T_d)+C_{14}\phi\frac{d\phi}{dt}\right] \quad (21)$$

The coupled differential equations, (20) and (21), were solved using MATLAB's ODE 45 solver for non-stiff problems. A time step size of $2.5 * 10^{-4}\ s$, temperature of 37° C, and 99.5% RH, corresponding to internal lung conditions, were applied (Longest et al., 2010). Estimating the initial salt water droplet diameter was done through determining the mass ratio of salt in the droplet, assuming the maximum salt solubility, and solving for droplet diameter. In water, the maximum solubility of salt is $\frac{36.6\ g\ NaCl}{100\ g\ H_2O}$ at 37°C. Through rearranging of (22), droplet diameter (ϕ) could be solved for. Note subscript p and w represent particle and water respectively. Given known salt particle density of 2.165 g/cc and water density of 1.00 g/cc, (22) was solved for the droplet diameter at saturation which equals $1.905\phi_p$. Thermal properties at 37°C were calculated from interpolation of tabulated data (Bergman et al., 2011), and the equations from curve fitting can be found in Table 7.

$$\frac{m_p}{m_p+m_w} = \frac{\phi_p^3\rho_p}{\left(\phi^3-\phi_p^3\right)\rho_w+\phi_p^3\rho_s} \quad (22)$$

For additional analysis, the differential equations were modified to account for temperature and RH variations. Table 8 shows the updated constant groups with temperature dependent properties removed. Varying temperature and RH reduces the number of constant groups to 8. Thermal property equations were acquired through curve

fitting of data from previously mentioned equations in Table 7. For properties that had negligible change with temperature, the value at 37°C was used. Through substitution of the constant groups into the original equations (10, 11, 14, 15, and 16) we arrived at the simplified equations (23-27) for solving for droplet diameter and temperature assuming varying temperature and humidity. Bolded values in the equations are temperature dependent.

$$a_d = a_w exp\left\{\frac{C_8\boldsymbol{\sigma(T_a)}}{\phi T_d} + C_9\boldsymbol{h_{fg}(T_a)}\left(\frac{1}{\boldsymbol{T_a}} - \frac{1}{T_d}\right)\right\} \quad (23)$$

$$\frac{d\phi}{dt} = \frac{C_6\boldsymbol{D_v^* p^s(T_a)}}{\phi\boldsymbol{\rho_d}}\left[\frac{\boldsymbol{RH}}{\boldsymbol{T_a}} - \frac{\boldsymbol{a_d}}{T_d}\right] \quad (24)$$

$$\frac{dT}{dt} = \frac{C_{11}}{\phi^2}\left[\frac{C_{12}\boldsymbol{k_v^*}}{\boldsymbol{\rho_d}}(T_a - T_d) + \boldsymbol{h_{fg}(T_a)}\phi\frac{d\phi}{dt}\right] \quad (25)$$

$$\boldsymbol{D_v^*} = \boldsymbol{D_v(T_a)}\left[\frac{1}{1+C_2/\phi} + \frac{C_5\boldsymbol{D_v(T_a)}}{\phi\sqrt{T_a}}\right]^{-1} \quad (26)$$

$$\boldsymbol{k_v^*} = \boldsymbol{k_v(T_a)}\left[\frac{1}{1+C_2/\phi} + \frac{C_3\boldsymbol{k_v(T_a)}}{\phi\boldsymbol{\rho_a(T_a)}\sqrt{T_a}}\right]^{-1} \quad (27)$$

Temperature and humidity profiles of the upper airways were obtained from a CFD data of heat and water transport throughout the lungs (Wu et al., 2015). Temperature and humidity data were fitted with polynomial functions shown below (28-29), and used for calculating temperature and humidity dependent properties in the differential equations. Previous application of this model assumed steady temperature and RH values.

$$T = \begin{cases} 304.57 + 14.90t + 74.80t^2 - 948.31t^3 + 3226.6t^4; & t < 0.241 \\ 310.15\,; & o.w. \end{cases} \quad (28)$$

$$RH = \begin{cases} 0.87 + 1.55t - 10.07t^2 + 43.44t^3 - 82.10t^4; & t < 0.22 \\ 0.995; & o.w. \end{cases} \quad (29)$$

HYGROSCOPIC GROWTH (EXPRIMENTAL METHODS)

AEROSOL GENERATION

A Collison three-jet nebulizer was used to atomize a distilled salt water solution. To reduce the number of particles produced, two of the jets were plugged to create a single jet nebulizer that produced a poly-disperse salt water aerosol. The salt water solution was made up of 2% salt by mass. The aerosol traveled through a heated metal pipe that acted as an evaporator before entering a condensing chamber. Fig. 15 displays the experimental schematic including the aerosol and salt crystal generating setup. The evaporation and condensation chambers in tandem removed the distilled water from the salt and produced pure salt crystals. The salt crystals were directed into a TSI Scanning Mobility Particle Sizer (SMPS). The TSI 3080 Electrostatic Classifier within the SMPS unit was configured to operate in mono-disperse mode, thus allowing a poly-disperse aerosol to enter, and a user defined mono-dispersed aerosol to exit. The SMPS created a mono-disperse aerosol using a TSI 3081 Differential Mobility Analyzer (DMA) Column. The DMA separated particle size by way of creating an electric field and taking advantage of the mobility of charged particles under the electric field. The mono-disperse generating capabilities were verified by Scanning Electron Microscopy (SEM) and calibration with a second SMPS. Fig. 16 shows SEM verification of a 400 nm salt particle generated by the mono-disperse creating SMPS. The SMPS mono-disperse creation abilities was calibrated against a second SMPS. Mono-disperse aerosols of 120 nm, 240 nm, and 360 nm were generated and measured with a second SMPS. The calibration plot can be seen in Fig. 17.

PARTICLE GROWTH REACTOR

Two different sized particle growth reactors were constructed to mimic the environmental conditions of the human lungs. The two reactors provide an opportunity to examine the transient effects of particle growth in human airways. Fig. 18 is a schematic of the large reactor. The reactor design was inspired by a similar design used in an experiment aimed at developing a standard for measuring hygroscopic particle growth (Li et al., 1992). The large reactor had a growth tube diameter of 0.0234 m, length of 0.909 m and allowed for a particle residence time of 0.8 seconds, while the small reactor allowed for a residence time of 0.22 seconds at a flowrate of 30.04 lpm, which corresponds to the average travel time of a particle from the mouth to the first bifurcation in the lungs (Longest et al., 2010). Residence time was defined as the average time a particle spends inside the reactor. The small reactors growth tube diameter and length were 0.0234 m and 0.259 m respectively. The reactors were composed of concentric tubes with two flow inlets and one flow outlet on the inner tube. The inner tube was a perforated metal tube that was wrapped in cloth with a plastic backing. The inner paper lining allowed for a saturated wall boundary. The whole tube was then covered with heat shrink polymer tubing to create a water tight seal around the exterior of the inner tube. The reactor allowed for isolation of the salt particles and humidified heated mixing air. The empty space between the concentric tubes in the reactor was filled with thermally conditioned water.

TEMPERATURE AND HUMIDITY CONTROL

Temperature was regulated within the growth reactor using a thermal water jacket. A temperature controlled water bath continuously pumped water heated to 39°C between

the concentric pipes. Additionally, 30 lpm of air was pushed through a water reservoir heated to 34.96°C and sent through the inner tube to simulate inspiration. This humid air stream mixed with the aerosol at the bottom of the inner tube. Humidity was controlled by a needle valve that controlled the amount of air entering the heated water reservoir. Humidity was measured in line prior to entering the reactor and at the reactor exit using a recently purchased Vaisala temperature and humidity probe. Excess air bypassed the water reservoir and reconnected with the humid air. By valve adjustment, the humidity could be controlled within less than ±0.5% relative humidity (RH). A schematic of the entire experimental setup can be seen in Fig. 15.

PARTICLE GROWTH MEASUREMENT

Final particle size was measured using a Grimm 164DM optical particle counter (OPC) Environmental Dust Monitor. This method of measurement allowed for quick measurements while also maintaining particle bin size resolution. Particle sizes were separated into 31 particle diameter bin sizes ranging from 0.25 µm to 32 µm. The instrument required 6 seconds for one complete measurement cycle. The OPC was calibrated by measuring PSL spheres that were manufactured to precise sizes. PSL spheres of 400 nm, 600 nm, 994 nm, and 2.2 µm were used for calibration. The OPC was accurate at 400 nm and 600 nm, but measurement error increased significantly with particle diameter, and the resulting calibration equation was a 3rd order polynomial equation that did not fit the measured PSL spheres well and can be seen in Fig. 19 (a). To adjust for this, the calibration equation was force fit to diameters below 400 nm, and the result was a 4th order polynomial that fit well in the diameter size range operating in. The calibration equation is shown in Fig. 19 (b). Additionally, a correction was applied to

account for the refractive index of salt water. It is known that OPC measurements of aerosols are often under measured compared to PSL sphere calibration measurements. This is due to light scattering differences due to refractive indices. Using particle diameter measurement data at different refractive indices from Liu and Daum (2000) and the refractive of salt being 1.35, corrected diameter data was interpolated and a calibration equation from curve fitting created. Fig. 20 shows the refractive index correction equation. Measurements were taken for 30 seconds and averaged to produce a single average measurement. To ensure measurements were capturing salt particles, measurements of only conditioned humid air were taken and subtracted out of the salt particle measurements to isolate the salt and remove unnecessary background measurements. This method was found to greatly increase the quality of the measurements.

Table 6: Constant groups for hygroscopic growth model assuming constant temperature and RH.

Constants Based on Grouping of Terms with Temperature of 37°C and 99.5% RH		
Constant	**Equation Affected**	**Constant Equation**
C1	Eq. 17, C3	k_v, Tsilingiris (2008)
C2	Eq. 17,18	$2\delta_t\lambda$
C3	Eq. 17	$\frac{2C1}{\alpha_t \rho_a c_{p,m} \sqrt{RT_a/2\pi M_a}}$
C4	Eq. 18, C5	D_v
C5	Eq. 18	$\frac{2C4}{\alpha_c \sqrt{RT_a/2\pi M_w}}$
C6	Eq. 20	$\frac{4M_w p^s(T_a)}{R}$
C7	Eq. 20	$\frac{RH}{T_a}$
C8	Eq. 19	$\frac{4M_w\sigma}{Rp_w}$
C9	Eq. 19	$\frac{h_{fg}M_w}{R}$
C10	Eq. 19	$\frac{1}{T_a}$
C11	Eq. 21	$\frac{3}{c_{p,w}}$
C12	Eq. 21	4
C13	Eq. 21	T_a
C14	Eq. 20	h_{fg}

Table 7: Thermal properties of air, water, water vapor and vapor-air mixtures.

Temperature Dependent Properties		
Property/Condition	**Dependence**	**Equation**
Miscellaneous Properties and Conditions		
Universal Gas Constant	Constant	N/A
Atmospheric Pressure	Assumed Constant	N/A
Molar Weight of Air	Constant	N/A
Molar Weight of Water Vapor	Constant	N/A
Water Activity**	N/A	$1 - 4.77 * 10^{-3}\left(\frac{m_p}{m_p + m_w}\right) - 1.65 * 10^{-4}\left(\frac{m_p}{m_p + m_w}\right)^2$
Dry Air Thermal Properties		
Viscosity	Yes	$4.72 * 10^{-8} T_a + 4.36 * 10^{-6}$
Specific Heat	Negligible	N/A
Thermal Conductivity	Yes	$7.38 * 10^{-5} T_a + 3.97 * 10^{-3}$
Density	Yes	$1.2 * 10^{-5} T_a^2 - 1.11 * 10^{-2} T_a + 3.44$
Saturated Water Vapor Properties		
Viscosity	Yes	$4.0 * 10^{-8} T_a - 2.91 * 10^{-6}$
Specific Heat	Negligible	N/A
Thermal Conductivity	Yes	$-2 * 10^{-6} T_a^2 + 0.013 T_a - 0.19$
Saturation Vapor Pressure	Yes	$\frac{exp\left(77.35 + 0.01 * T_a - {}^{7235}/_{T_a}\right)}{T_a^{8.2}}$
Diffusivity of Vapor in Air	Yes	$2.59 * 10^{-10} * T_a^2 + 1.04 * 10^{-8} * T_a - 7.81 * 10^{-7}$
Saturated Liquid Water Properties		
Latent Heat of Condensation	Yes	$2500.8 - 2.36(T_a - 273.15) + 0.002(T_a - 273.15)^2 - 0.0001(T_a - 27.13)^3$
Specific Heat	Negligible	N/A
Surface Tension	Yes	$235.8 * 10^{-3} * \left[\frac{647.15 - T_a}{647.15}\right]^{1.26} * \left[1 - 0.63 * \left(\frac{647.15 - T_a}{647.15}\right)\right]$
Density	Negligible	N/A
Vapor-Air Mixture		
Specific Heat	Negligible	Tsilingiris (2008)
Thermal Conductivity	Yes	Tsilingiris (2008)

Table 8: Constant groups for hygroscopic growth model assuming temperature and humidity profiles from (28) and (29).

Constants Based on Grouping of Temperature Independent Terms in Eq. 8-11		
Constant	**Eq. Affected**	**Constant Equation**
C2	Eq. 26, 27	$2\delta_t * \lambda$
C3	Eq. 27	$\frac{2}{\alpha_t * c_{p,m}\sqrt{R/(2\pi * M_a)}}$
C5	Eq. 26	$\frac{2}{\alpha_c\sqrt{R/(2\pi * M_w)}}$
C6	Eq. 24	$\frac{4M_w}{R}$
C8	Eq. 23	$\frac{4M_w}{R * \rho_w}$
C9	Eq. 23	$\frac{M_w}{R}$
C11	Eq. 25	$\frac{M_w}{R}$
C12	Eq. 25	$\frac{3}{c_{p,w}}$

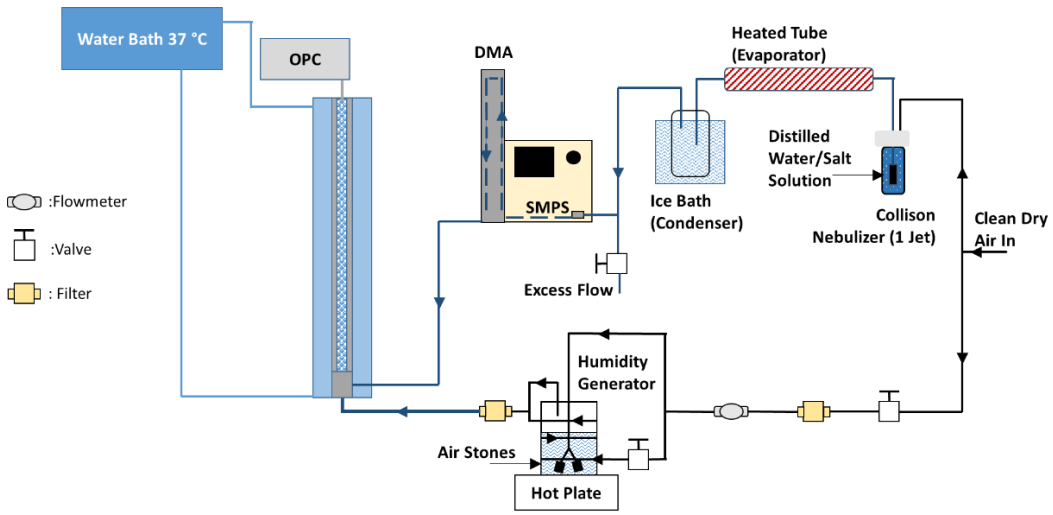

Figure 15: Schematic of the experimental setup.

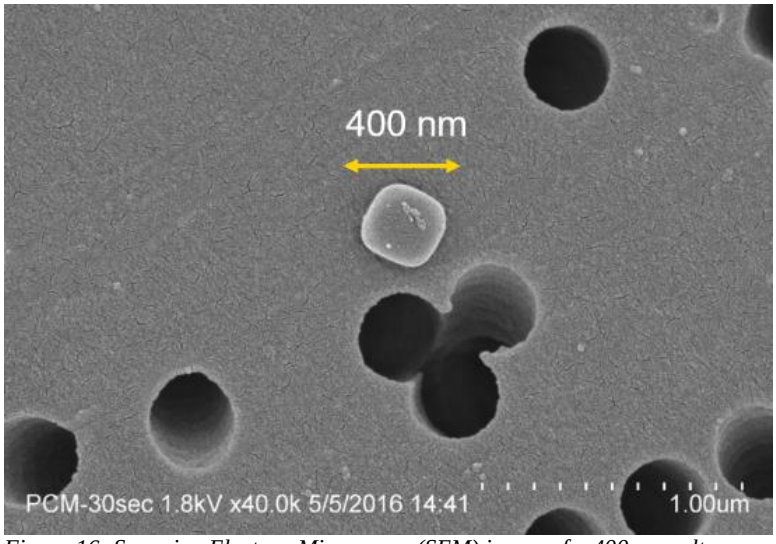

Figure 16: Scanning Electron Microscopy (SEM) image of a 400 nm salt particle produced by the mono-disperse SMPS aerosol generator.

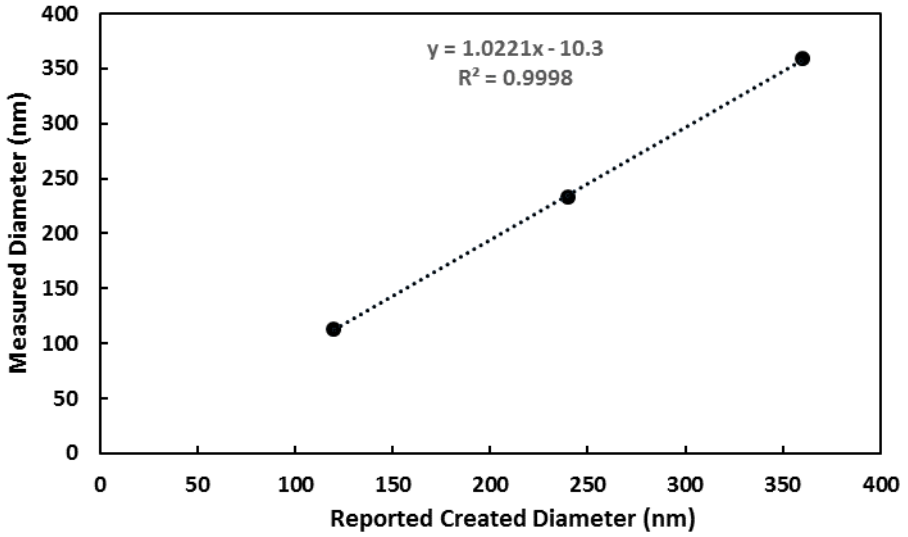

Figure 17: SMPS calibration plot. Mono-disperse aerosols of sizes 120, 240, and 360 nm are created to and measured with a dual SMPS setup.

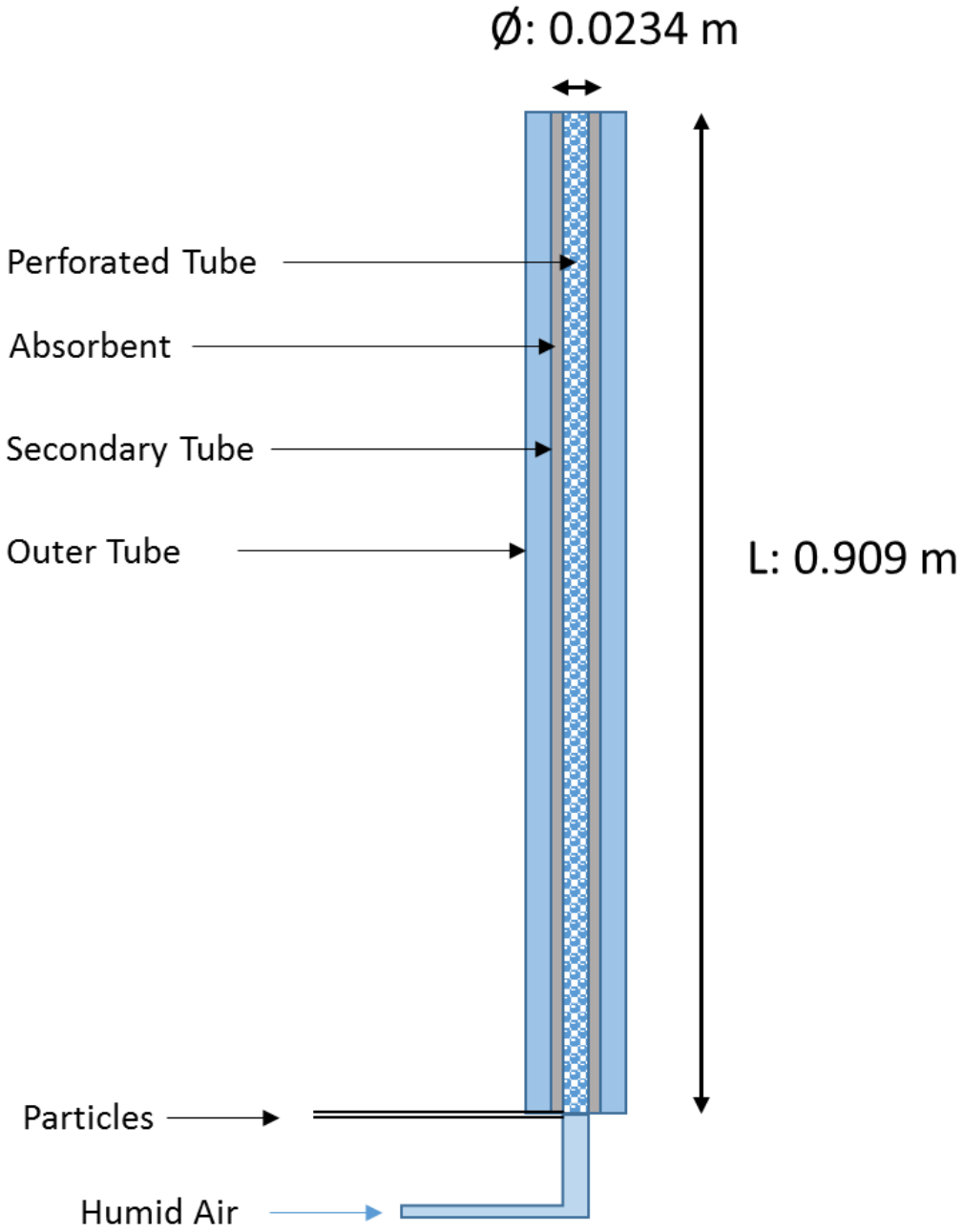

Figure 18: Large growth reactor schematic with major dimensions.

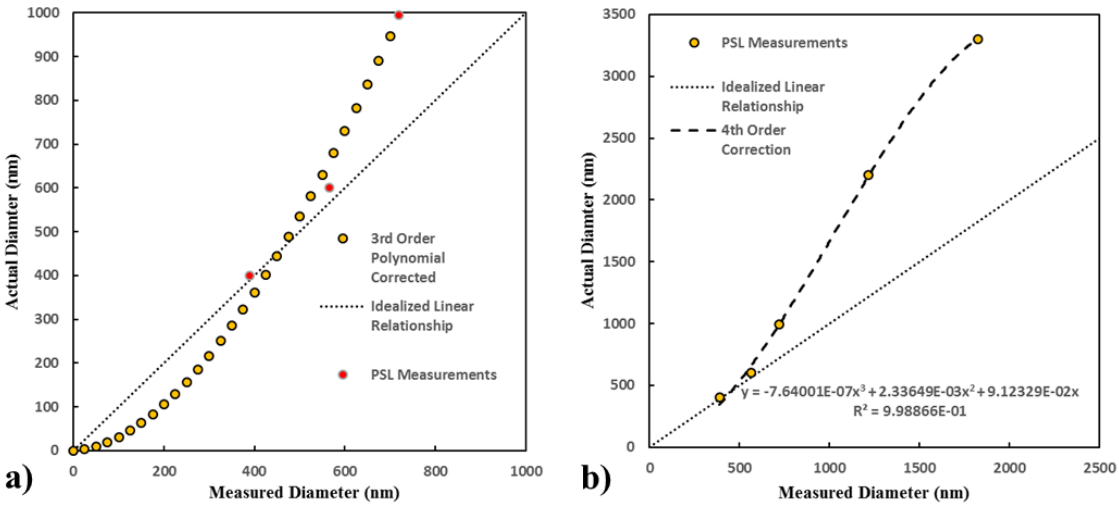

Figure 19: PSL sphere calibration curve for (a) 3rd order polynomial, and (b) 4th order polynomial created from force fitting points below 400 nm.

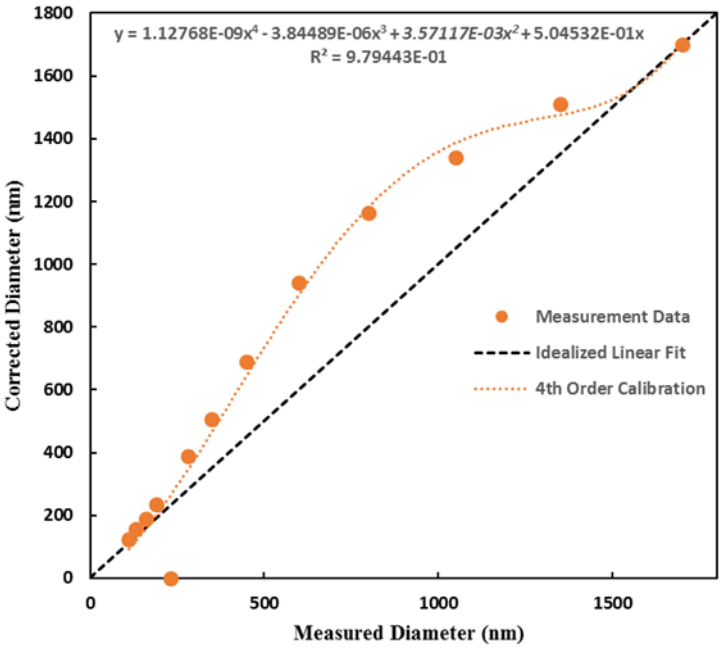

Figure 20: OPC refractive index calibration for salt water measurement.

RESULTS

MODEL RESULTS

Using the constant temperature and RH model, with RH and temperature values corresponding to the *in vitro* model environment, droplet growth was approximated for various salt particle sizes over a 10 second range and presented in Fig. 21 Droplet growth was presented as the ratio of droplet diameter over initial salt particle diameter. Model results show that steady state droplet size is not achieved for micron sized initial particles after 10 seconds. 500 nm particles do not reach steady state size until after 5 seconds in which point the diameter fluctuates by 0.1 nm. 100 nm particles reach final growth size within 0.2 seconds, which corresponds to the average travel time of air to the first bifurcation of the lungs (Longest et al., 2010). It is worth noting that particle size approximately doubles instantaneously. This was a result of the assumption that growth does not happen until after a particle turns into a homogenous saturated salt water droplet. The estimation of initial droplet size is unique to this presentation and was not adapted from Broday & Georgopoulos (2001). After 0.2 seconds, from the initial droplet sizes, the 5 µm particle had only grown by 20.8% and 10 µm particle by 11.0% µm. This is compared to 1 µm, 0.5 µm, and 0.1 µm which had grown by 88.9%, 128.6%, and 160.1% respectively. Fig. 21 (b) shows the same growth plots but over a 0.2 second range. The lack of diameter change by the 5 µm and 10 µm can be visualized easily. Particle sizes at various points in time were presented for each initial particle size in Table 9. Steady state diameter predictions for various initial diameters were obtained using the model at 37 ° C and 99% RH, and compared to *in vitro* TDMA experimental data at the same conditions from Li et al., (1992) in Fig. 22. The model showed good

agreement with the experimental data for steady state growth ratio predictions, especially at initial diameter sizes less than 75 nm. Using the variable temperature and RH model, growth curves for various droplet sizes were plotted with associated constant condition curves for comparison in Fig. 23. A time lag can be seen for the variable condition model results. The time lag increased with initial droplet size. Droplet size for the variable model was considered converged when the growth factor was within 0.1 of the constant model. This occurred at 0.57 seconds, 0.72 seconds, and 0.75 seconds for 300 nm, 500nm, and 700 nm cases respectively. Variable and steady growth curves for a 700 nm initial salt water droplet sizes were compared with acquired *in vivo* data of the same initial diameter from Anselm et al. (1986) in Fig. 24. Both models had good agreement with the *in vivo* data after 1.25 seconds. Prior to 1.25 seconds, both models were considerable different from the experimental data.

HYGROSCOPIC GROWTH GRIMM OPC MEASUREMENTS

The Grimm OPC final droplet diameters were measured and stored as a cumulative distribution. Data was separated and plotted as a histogram. To determine the final size, the count median diameter (CMD) was computed (Hinds, 1999). To reduce error, the CMD was only calculated over the three largest adjacent bins in the distribution. This was determined an appropriate method for data refinement. OPC measurements were sometimes bimodal, with a large particle count in the first few size channels, and this would result in the CMD being heavily skewed from the true value. Bimodal distributions resulted from averaging out water vapor measurements. Fig. 25 shows the OPC data output histograms after subtraction of water vapor measurements. Note the x-axis uses a logarithmic scale. Table 11 presents the CMD values before and

after calibration adjustments. For 600 nm, and 800 nm initial diameters the final diameter size for the long reactor was larger than the corresponding short reactor measurements. For 400 nm initial diameter size, the large reactor measured 567.39 nm for the final size, and the short reactor measured 625.21 nm. This was the only instance where final size was smaller for the large reactor. The differences in final measured size between reactors increased with initial particle size.

COMPARISON OF MODEL AND EXPERIMENTAL RESULTS

Hygroscopic growth was modeled for 400 nm, 600 nm, and 800 nm corresponding to the initial particle sizes measured in the *in vitro* experiment. The two reactors correspond to 0.22 s and 0.84 seconds on the model growth curve. Experimental data was plotted with the model output for comparison. The experimental data did not match well with the model results. Measurement and model differences increased with initial particle size for the short reactor, while the large reactor had enormous error at the 400 nm, error reduced slightly to approximately 97% for the 600 nm and 800 nm initial diameter measurement trials. Table 11 presents the experimental measured final diameters, corresponding growth model diameters, and percent difference between. Fig. 26 (a, b) displays the measurement data and model results for the same particle sizes. At first glance, it appeared the measurement data trends are like the model results just much lower in magnitude. To analyze the trend of the data, the 800 nm experimentally measured data point was force fit to the model curve, and the ratio between the model diameter and experimental diameter at 0.84 seconds for 800 nm was multiplied to the remaining experimentally measure data points. The results showed better agreement with the model, however this correction cannot be substantiated and was performed under the

assumption that the forced fit point is the actual diameter at 0.84 seconds. Fig. 26 (a) shows the modified plot. Model results were then obtained through the model equations that account for temperature and humidity variations. Fig. 27 shows the constant temperature and humidity model output, variable temperature and humidity output, and experimental data for comparison.

Table 9: Droplet diameter sizes at different time points. Data reported is from the steady temperature and RH model.

Diameter/Time	0.1 µm	0.5 µm	1 µm	5 µm	10 µm
0.3125 s	0.49632 µm	2.329 µm	3.879 µm	12.211 µm	21.195 µm
0.625 s	0.49634 µm	2.554 µm	4.343 µm	13.385 µm	22.507 µm
1.25 s	0.49636 µm	2.735 µm	4.818 µm	14.900 µm	24.440 µm
2.5 s	0.49634 µm	2.837 µm	5.264 µm	16.682 µm	26.932 µm
5 s	0.49645 µm	2.866 µm	5.613 µm	18.708 µm	27.979 µm
10 s	0.49635 µm	2.867 µm	5.804 µm	20.942 µm	33.554 µm

Table 10: 3 bin CMD measurements for short and long reactors with adjusted values based on calibrations.

Short Reactor (0.22 sec. residence time)		
Initial Diameter	OPC Measured CMD	Adjusted CMD
400 nm	625.21 nm	1128.15 nm
600 nm	877.26 nm	1472.63 nm
800 nm	1472.61 nm	1532.47 nm
Long Reactor (0.84 sec. residence time)		
Initial Diameter	OPC Measured CMD	Adjusted CMD
400 nm	567.40 nm	1000.93 nm
600 nm	968.87 nm	1562.52 nm
800 nm	1126.24 nm	1958.99 nm

Table 11: Comparison of experimental and model final diameter results.

0.22 second residence time			
Initial Diameter	Experimental Final Diameter	Model Final Diameter	Percent Difference
400 nm	1128.15 nm	1869.40 nm	65.7%
600 nm	1472.63 nm	2540.61 nm	72.5%
800 nm	1532.47 nm	3129.02 nm	104.2%
0.84 second residence time			
Initial Diameter	Experimental Final Diameter	Model Final Diameter	Percent Difference
400 nm	1000.93 nm	2183.25	118.1%
600 nm	1562.52 nm	3082.65	97.3%
800 nm	1958.99 nm	3858.70	97.0%

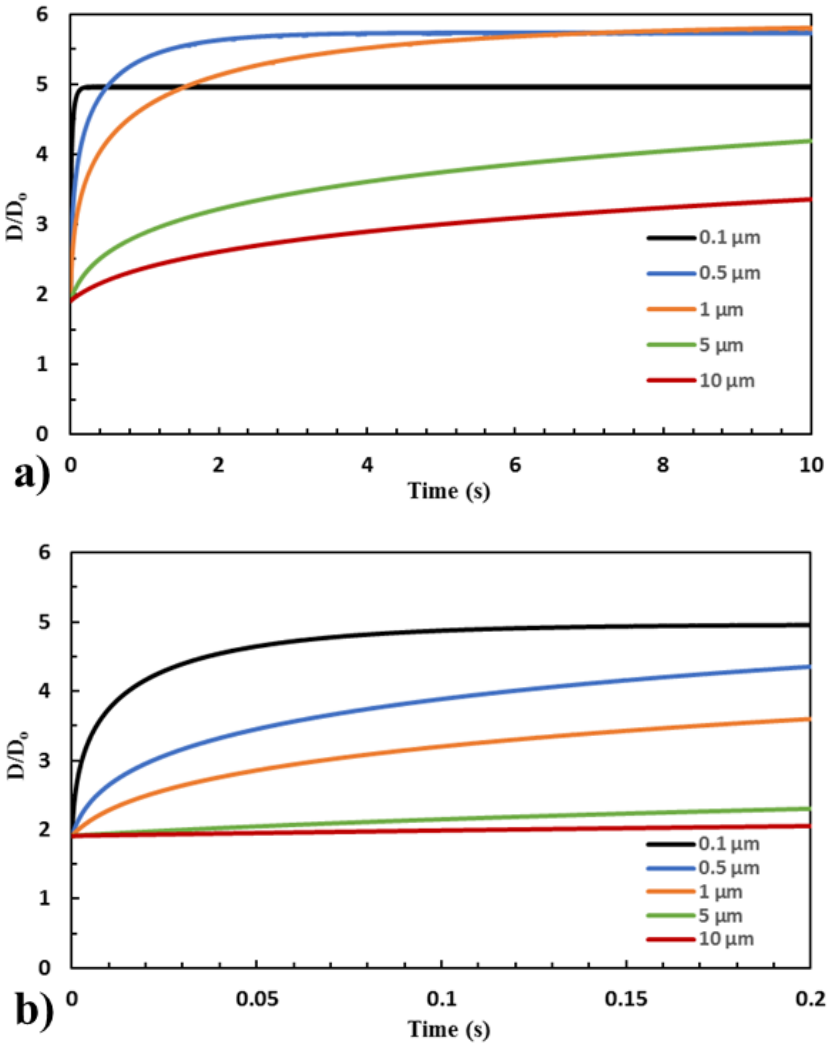

Figure 21: Model results for droplet growth of various initial particle sizes over growth time intervals of (a) 10 seconds and (b) 0.2 seconds.

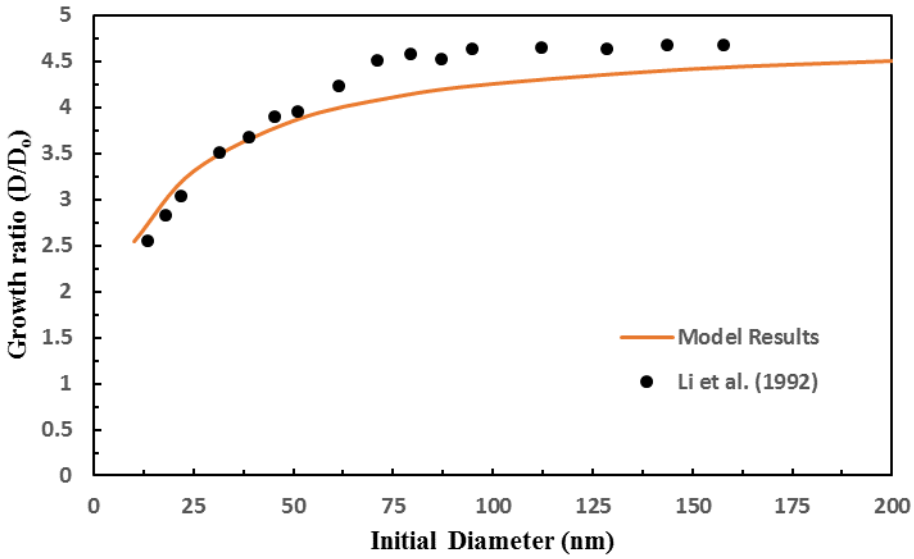

Figure 22: Comparison of the model output with experimental data taken at 99.5% RH and 37 ° C.

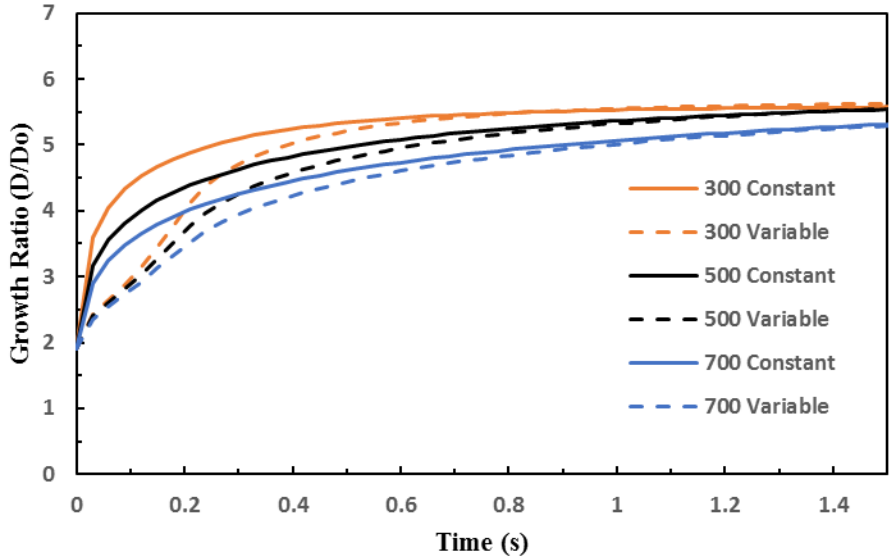

Figure 23: Variable temperature and RH compared to constant 37 °C and 99.5 RH.

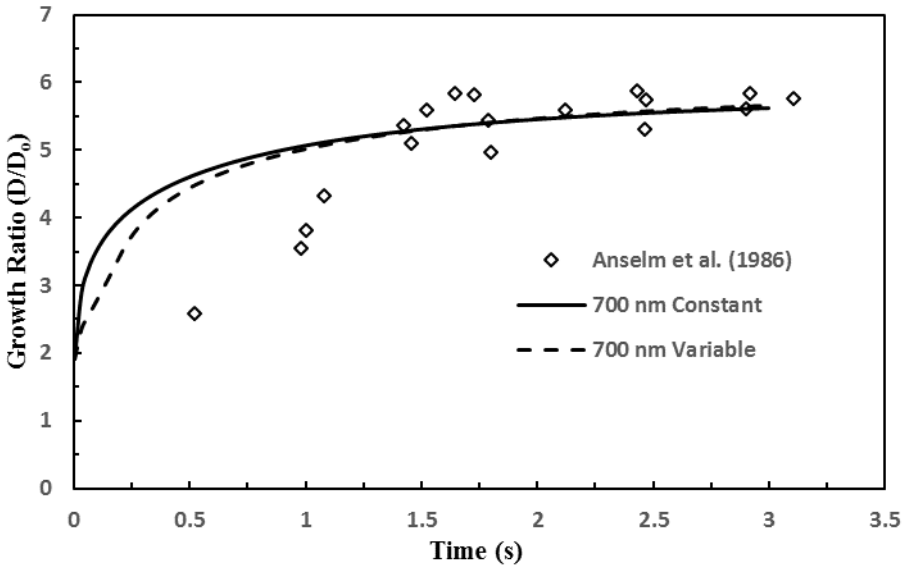

Figure 24: Comparison of variable and constant temperature and RH models with in vivo data.

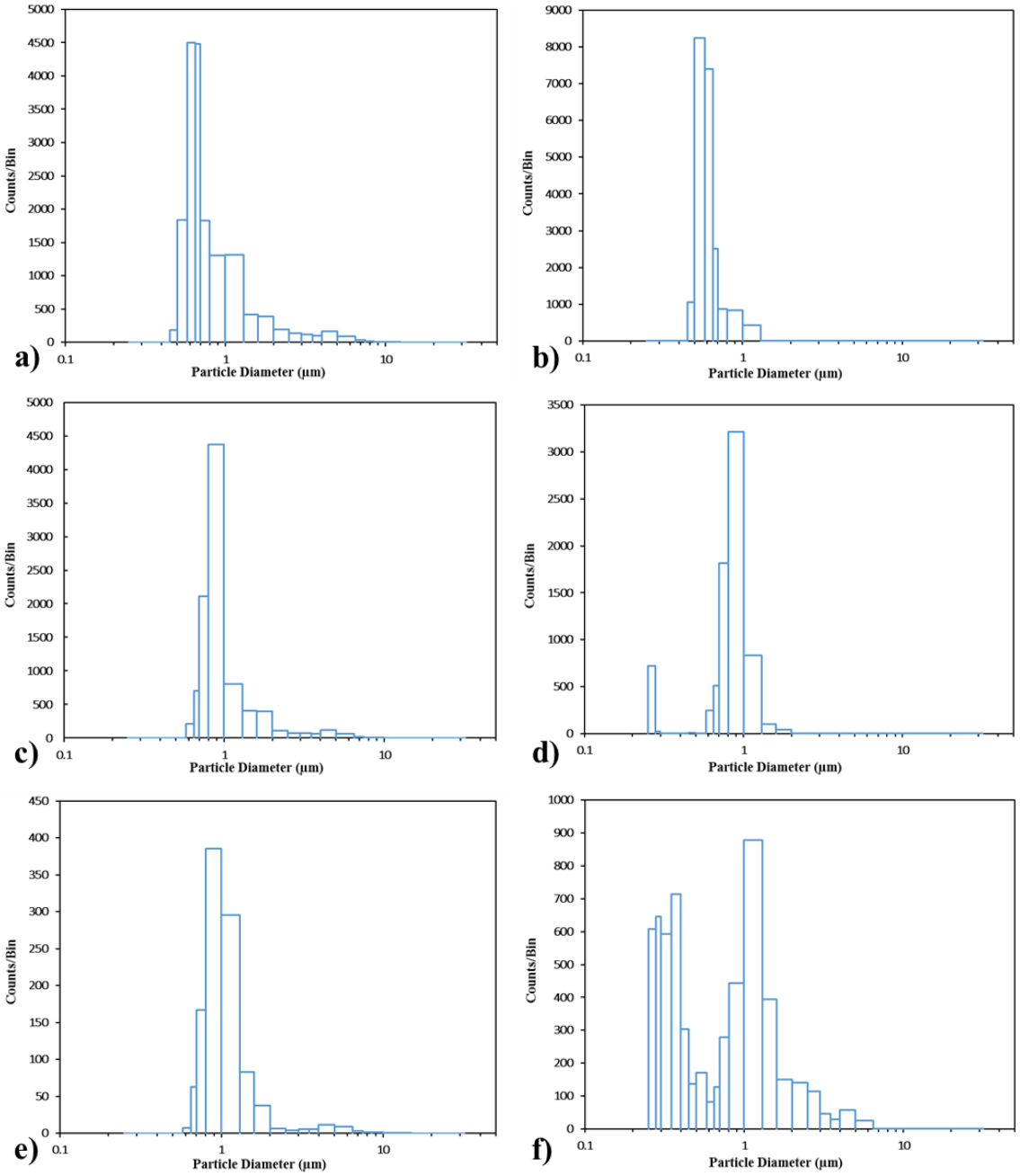

Figure 25: OPC final droplet growth measurements for (a, c, e) 0.22 s residence time for 400 nm, 600 nm, and 800 nm respectively and (b, d, f) 0.84 s residence time for 400 nm, 600 nm, and 800 nm respectively.

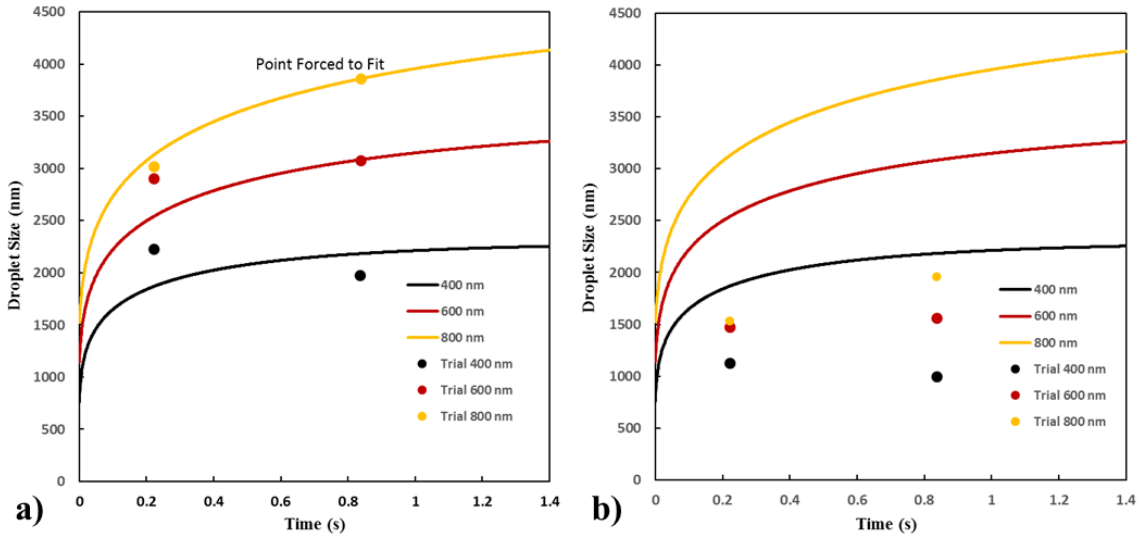

Figure 26: a) OPC measured experimental growth data plotted with model results at 400 nm, 600 nm, and 800 nm initial diameters, b) corrected measurement data assuming the measured 800 nm final diameter at 0.84 seconds is force fit to the model.

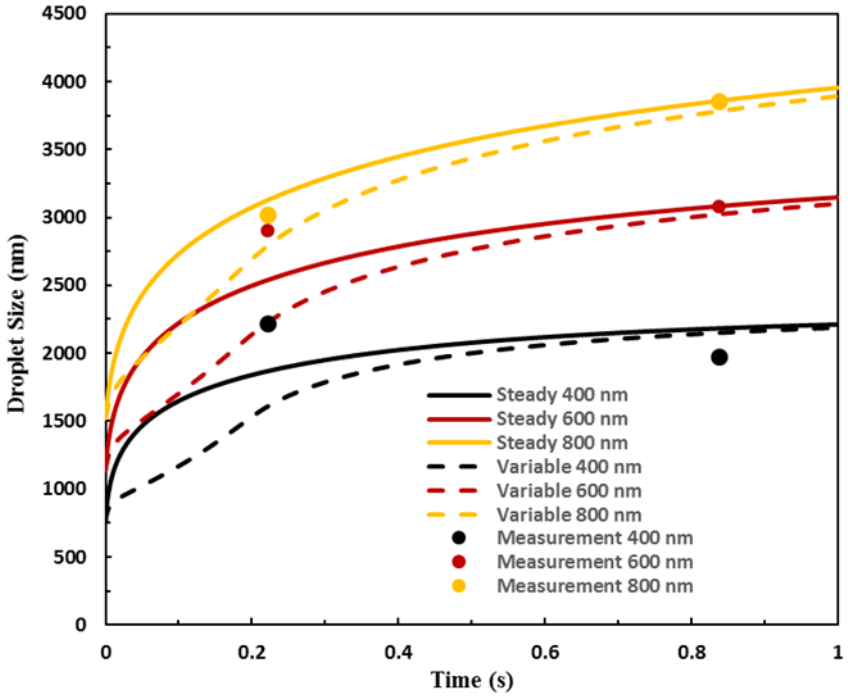

Figure 27: Growth model using constant temperature, 37 °C, and RH, 99.5%, and variable temperature and RH.

DISCUSSION

When comparing the measurement data to the model output, it appears the data follows the model growth trend, but is translated lower, like the possibility of a time lag existing prior to growth commencing. One major assumption that the growth models make is the initial condition is not a pure salt particle, rather a homogenous salt-water droplet solution that can begin growing instantaneously (Asgharian, 2004; Broday & Georgopoulos, 2001; Ferron et al., 1988). This is in fact not true. There exists a phase in which a salt particle in a humid environment is the site of nucleation for which a droplet forms via condensation. This phenomenon is called deliquescence and literature on the topic is limited to measurement of critical RH values to commence deliquescence. These studies revolve around measurement of nanometer sized particles less than 200 nm (Mauer & Taylor, 2010; Biskos 2006). One theory for the disagreement between the model and experimental measurements is a time delay for deliquescence exists, where the amount of time increases with initial particle size.

Typically, researchers utilize the dual differential mobility analysis setup, sometimes referred to as tandem differential mobility analysis, to measure hygroscopic growth (Biskos, 2006; Li et al, 1992). It allows for precision mono-disperse generation capabilities and measurement. However, the residence time within these instruments and setups can be greater than 10 seconds, negating an attempt to capture transient nature of growth, and deliquescence. This issue was mentioned in Biskos (2006). Additionally, the high flowrate necessary to replicate pulmonary in-vitro experiments hinders the measurement abilities of the DMA to final sizes less than 300 nm. Based on numerical model outputs in Fig. 21, Fig. 23, and initial particle sizes of interest, greater than 300

nm, HDDMA setups cannot even accommodate measuring the steady state sizes due to the high flowrates in the experiment that correspond to asthma inhaler inhalation. Based on the small particle sizes measured and long residence time, it is possible that in Li et al. (1992) deliquescence is not addressed, nor needed to be considered because there was adequate time for their salt particles to fully deliquesce into droplets and grow to their final size. Initially, the HDDMA method was employed for this experiment, but the small particle sizes, and lengthy residence time were not applicable to the scope of the research. Targeted drug delivery by means of dynamically sized particles through hygroscopic growth requires visualization of the time history of diameter growth. Typical pharmaceutical drugs are between 1 – 5 μm (Mitchell et al., 2003; Walenga & Longest, 2016), and it is well known that particles greater than 4 μm have large deposition losses in the mouth and throat regions, while submicron particles have upwards of 70% of the aerosol exhaled back out. Additionally, the residence time from the throat to first lung bifurcation in the average male is 0.2 seconds (Longest et al., 2010), therefore measurement instruments must be quick. It for these reasons that application of hygroscopic particle growth for pharmaceutical purposes has utilized instruments with coarser resolution for particle measurement such as OPC and ACI. Ultimately, an OPC was settled on for instrument selection because ACI measurement stages are two large for any sort of diameter size accuracy (Longest et al., 2010).

Another area for uncertainty in the growth model is the assumption that temperature and RH remain constant when in fact they vary spatially, as presented by the numerical data of temperature and water vapor profile obtained from (Wu et al., 2015). In the temperature profile acquired, RH began at 88.5% and did not reach 99.5% until 0.241

seconds which agrees with the humidity profile used by Winkler-Heil et al. (2014). Per Biskos (2006), growth of 60 nm particles does not have a noticeable effect until 80% RH. With larger particles requiring more extreme conditions for deliquescence and rapid growth, an additional time lag is possible due to spatial humidity gradients. The time varying temperature and RH model confirms that a delay in growth is present resulting from temperature and humidity gradients in the lungs. Fig. 23 showed that time lag for growth increased with particle size. This results from more vapor diffusion being required onto the droplet for growth. The varying conditions curves are more realistic representations of breathing in a hygroscopic particle. The model still lacks information pertaining to time required for a dry particle to deliquesce to a droplet before growth commencement.

Ferron et al. (1988) observed that growth was highly dependent on flowrate. Particles less than 1 μm in initial size grew much more rapidly when inhaled at 45 lpm compared to 15 lpm. This could result from particle reaching critical humidity to facilitate growth faster. This could be an important area for future work, as inhalation flowrates in people is highly variable. Achieving targeted drug delivery would require precise control over inhalation flowrate.

CONCLUSIONS

This study presented and explained a model initially developed by Broday & Georgopoulos (2001) for predicting growth of a hygroscopic salt particle with the application of droplet growth in the human respiratory tract. This study expands upon the original growth model and attempts to further increase the accuracy of the model by incorporating temperature and humidity profiles corresponding to 0.2 seconds of

residence time in the lungs from a previously published study. Validation attempts through an *in vitro* experiment were unsuccessful, and showed disagreement with the model and data results. The experimental data was more than 65% different than predicted model results. When experimental data was corrected to force fit a data point to the model curve, the experimental data showed a trend that agreed with predicted values.

The disagreement in the data suggests that there is a delay in growth associated with spatial temperature and humidity gradients and the deliquescence process. Research in this area focuses on the steady state final particle size (Asgharian, 2004; Biskos et al., 2006; Li et al., 1992). In the case of Li et al. (1992) and Biskos et al. (2006), the experimental measurement devices used have slow sampling times allowing sufficient time for steady state to be reached. Comparison with data from Anselm et al. (1986) and Winkler-Heil et al. (2014) confirm that a time delay exists.

There is an interest in the idea of engineering dynamically sized pharmaceuticals for target delivery in the lungs (Longest et al., 2010; Longest et al., 2011; Longest & Hindle, 2011; Son et al., 2013; Tian et al, 2010; Winkler-Heil et al., 2014). Due to the lack of understanding of deliquescence, small particle sizes, and short residence times associated with breathing, it is imperative that an understanding of deliquescence, and the time delay required for a particle to turn into a homogenous salt water droplet, is acquired so that accurate growth models can be developed for predicting drug deposition locations. Future studies could focus on capturing deliquescence and incorporating the process of a salt transforming into a droplet into the growth models and validating through experimental measurements. This would be a novel finding as growth models currently assume droplet status as an initial condition. Additionally, once model validation is

achieved, incorporating the growth model into the LES CFD and particle tracking model described previously in conjunction with the cluster analysis would be a large step in developing subject specific targeted drug delivery using dynamically sized particles.

REFERENCES

Anselm, A., Gebhart, J., & Heyder, J. (1986). Human inhalation studies of growth of hygroscopic particles in the respiratory tract. *2nd International Aerosol Conference* (pp. 252-255). Berlin: Pergamon Journals Ltd.

Asgharian, B. (2004). A model of deposition of hygroscopic particles in the human lung. *Aerosol Science and Technology, 38*, 938-947.

Barbosa-Cánovas, G. V., Fontana, A. J., Schmidt, S. J., & Labuza, T. P. (2008). *Water activity in foods: Fundamentals and applications.* Ames, IA: Wiley-Blackwell.

Bergman, T. L., Lavine, A. S., Incropera, F. P., & DeWitt, D. P. (2011). *Fundamentals of heat and mass transfer.* (7, Ed.) Wiley & Sons.

Biskos, G., Paulsen, D., Russel, L. M., Buseck, P. R., & Martin, S. T. (2006). Prompt deliquescence and efforescence of aerosol nanoparticles. *Atmospheric Chemistry and Physics, 6*, 4633-4642.

Borgstrom, L., Olsson, B., & Thorsson, L. (2006). Degree of throat deposition can explain the variability in lung deposition of inhaled drugs. *Journal of Aerosol Medicine, 19*, 473-483.

Bos, A. C., van Holsbeke, C., de Backer, J. W., van Westreenen, M., Janssens, H. M., Vos, W. G., . . . Tiddens, M. (2015). Patient-specific modeling of regional antibiotic concentration levels in airways of patients with cyctic fibrosis: Are we dosing high enough? *PLoS ONE, 10*, 1-21.

Broday, D. M., & Georgopoulos, P. G. (2001). Groth and deposition of hygroscopic particulate matter in the human lungs. *Aerosol Science and Technology, 34*, 144-159.

Byron, P. (2004). Drug delivery devices: Issues in drug development. *Proceedings of the American Thoracic Society, 1*, 321-328.

Castro, M. S., Fain, S. B., Hoffman, E. A., Gierada, D. S., Erzurum, S. C., & Wenzel, S. (2011). Lung imaging in asthmatic patients: the picture is clearer. *Journal of Allergy and Clinical Immunology, 128*, 467-478.

Cheng, Y. S. (2014). Mechanisms of pharmeceutical aerosol deposition in the respiratory tract. *AAPS Pharmeceutical Science and Technology, 15*, 630-640.

Choi, J., Tawhai, M. H., Hoffman, E. A., & Lin, C.-L. (2009). On intra- and intersubject variabilities of airflow in the human lungs. *Phys. Fluids, 21*(10), 101901.

Choi, S., Choi, J., Miyawaki, S., Hoffman, E. A., & Lin, C.-L. (2016, May 13-18). Improved estimations of flow distributions using a 1-D resistance network model in asthmatic airways. *American Thoracic Society Annual Meeting.* San Francisco, CA.

Choi, S., Hoffman, E. A., Wenzel, S. E., Castro, M., Fain, S. B., Jarjour, N. N., . . . Lin, C.-L. (2015). Quantitative assessment of multiscale structural and functional alterations in asthmatic populations. *Journal of Applied Physiology, 118*, 1286-1298.

Choi, S., Hoffman, E. A., Wenzel, S. E., Castro, M., Fain, S., Jarjour, N., . . . Lin, C.-L. (2017). Quantitative computed tomography imaging-based clustering differentiates asthmatic subgroups with distinctive clinical phenotypes. *Journal of Allergy and Clinical Immunology*.

Cosio Piqueras, M. G., & Cosio, M. G. (2001). Disease of the airways in chronic obstructive pulmonary disease. *European Respiratory journal, 18*, 41s-49s.

Crowe, C. T., Chung, T. N., & Troutt, T. (1988). Particle mixing in free shear flows. *Progress in Energy and Combustion Science, 14*, 171-194.

Crowe, C. T., Gore, R. A., & Troutt, T. R. (1985). Particle dispersion by coherent structures in free shear flows. *Particulate Science and Technology, 3*, 149-158.

De Backer, J. W., Vos, W. G., Vinchurkar, S. C., Claes, R., Drollmann, A., Wilfrank, D., . . . De Backer, W. (2010). Validation of computational fluid dynamics in CT-based airway models with SPECT/CT. *Radiology, 257*, 854-862.

Fadl, A., Wang, J., Zhang, Z., & Cheng, Y. S. (2007). Effects of MDI spray angle on aerosol penetration efficiency through an oral airway cast. *Journal of Aerosol Science, 38*(8), 853-864.

Ferron, G. A. (1977). The size of soluable aerosol particles as a function of the humidity of the air: application to the human respiratory tract. *Journal of Aerosol Science, 3*, 251-267.

Ferron, G. A., Kreyling, W. G., & Haider, B. (1988). Inhalation of salt aerosol particles II. Growth and deposition in the human respiratory tract. *Journal of Aerosol Science, 19*, 611-631.

Friedlander, S. K., Windeler, R. S., & Weber, A. P. (1994). Ultrafine particle formation by aerosol processes in turbulent jets: Mechanisms and scale up. *Nanostructured Materials, 4*(5), 521-528.

Heistracher, T., & Hofmann, W. (1995). Physiologically realistic models of bronchial airway bifurcations. *Journal of Aerosol Science, 26*, 497-509.

Heyder, J., Gebhart, J., Rudolf, G., Schiller, C. F., & Stahlhofen, W. (1986). Deposition of particles in the human respiratory tract in the size range of 0.005-15 microns. (5, Ed.) *Journal of Aerosol Science, 17*, 811-825.

Hinds, W. C. (1999). *Aerosol technology: Properties, behavior, and measurement of airborne particles.* Hoboken, NJ: John Wiley & Sons.

Horsfield, K., Dart, G., Olson, D., Filley, G., & Cumming, G. (1971). Models of the human bronchial tree. *Journal of Applied Physiology, 31*, 207-217.

Jaques, P. A., & Kim, C. S. (2000). Measurement of total lung deposition of inhaled ultrafine particles in healthy men and women. *Inhalation Toxicology, 12*, 715-731.

Khorasanizade, S., Shams, M., & Mansoori, B. M. (2011). Calculation of aerosol deposition in human airways using Horsfield geometric model. *Advanced Powder Technology, 22*, 695-705.

Kim, C. S., Eldridge, M. A., Garcia, L., & Wanner, A. (1989). Aerosol deposition in the lung with assymetric airway obstruction: in vivo observation. *Journal of Applied Physiology, 67*(6), 2579-2585.

Kitic, D., Pereira Jardim, D. C., Favetto, G. J., Resnik, S. L., & Chirife, J. (1986). Theoretical prediction of the water activity of standard saturated salt solutions at various temperatures. *Journal of Food Science, 51*, 1037-1041.

Lambert, A. R., O'Shaugnessy, P. T., Tawhai, M. H., Hoffman, E. A., & Lin, C.-L. (2011). Regional deposition of particles in an image-based aiway model: Large-eddy simulation and left-right lung ventilation asymmetry. *Aerosol Science and Technology, 45*, 11-25.

Li, W., Montassier, N., & Hoepke, P. K. (1992). A system to measure hygroscopicity of aerosol particles. *Aerosol Science and Technology, 17*, 25-35.

Lin, C.-L., Lee, H., Lee, T., & Weber, L. J. (2005). A level set characteristic galerkin finite element method for free surface flows. *Int. J. Numer. Methods Fluids, 49*, 521-548.

Lin, C.-L., Tawhai, M. H., McLennon, G., & Hoffman, E. A. (2009). Multiscale simulation of gas flow in subject specific models of the human lung. *IEEE Engineering in Medicine and Biology, 28*, 25-33.

Liu, Y., & Daum, P. H. (2000). The effect of refractive index on size distributios and light scattering coefficients derived from optical particle counters. *Journal of Aerosol Science, 31*, 945-957.

Longest, P. W., & Hindle, M. (2010). CFD simulations of enhanced condensational growth (ECG) applied to respiratory drug delivery with comparisons to in vitro data. *Journal of Aerosol Science, 41*, 805-820.

Longest, P. W., & Hindle, M. (2011). Numerical model to characterize the size increase of combination drug and hygroscopic excipient nanoparticle aerosols. *Aerosol Science and Technology, 45*, 884-899.

Longest, P. W., & Hindle, M. (2012). Condensational growth of combination drug-excipient submicrometer particles for targeted high efficiency pulmonary delivery: Comparison of CFD predictions with experimental results. *Pharmeceutical Research, 29*, 707-721.

Longest, P. W., McLeskey Jr., J. T., & Hindle, M. (2010). Characterization of nanoaerosol size change during enhanced condensational growth. *Aerosol Science and Technology, 44*, 473-483.

Longest, P. W., Tian, G., & Hindle, M. (2011). Improving the lung delivery of nasally administered aerosols during noninvasice ventilation: An application of enhanced condensational growth (ECG). *Journal of Aerosols, 24*, 103-118.

Longest, P. W., Tian, G., Walenga, R. L., & Hindle, M. (2012). Comparing MDI and DPI aerosol deposition using in vitro experiments and a new stochastic individual path (SIP) model of the conducting airways. *Pharmeceutical Research, 29*, 1670-1688.

Martonen, T., Fleming, J., Schroeter, J., Conway, J., & Hwang, D. (2003). In silico modeling of asthma. *Advanced Drug Delivery Reviews, 55*, 829-849.

Mauer, L. J., & Taylor, L. S. (2010). Water-solids interactions: deliquescence. *Annual Review of Food Science and Technology, 1*, 41-63.

Maxey, M. R., & Riley, J. J. (1983). Equation of motion for a small rigid sphere in a nonuniform flow. *Fluids, 26*, 883-889.

McMurry, P. H. (2000). A review of atmospheric aerosol measurements. *Atmospheric Environment, 34*, 1959-1999.

Mitchell, J. P., Nagel, M. W., Wiersema, K. J., & Doyle, C. C. (2003). Aerodynamic particle size analysis of aerosols from pressurized metered-dose inhalers: Comparison of andersen 8-stage cascade impactor, next generation pharmeceutical impactor, and model 3321 aerodynamic particle sizer aerosol spectrometer. *AAPS Pharmeceutical Science and Technology, 4*, 1-9.

Miyawaki, S., & Lin, C.-L. (2017). Numerical simulations of aerosol delivery to the human lung with an idealized laryngeal model, image-based airway model, and automatic meshing algorithm. *Computers and Fluids, 148*, 1-9.

Miyawaki, S., Hoffman, E. A., & Lin, C.-L. (2016). Effect of static vs. dynamic imaging on particle transport in CT-based numerical models of human central airways. *Journal of Aerosol Science, 100*, 129-139.

Miyawaki, S., Tawhai, M. H., Hoffman, E. A., Wenzel, S. E., & Lin, C.-L. (2017). Automatic construction of subject-specific human airway geometry including trifurcations based on a CT-segmented airway skeleton and surface. *Biomechanics and Modeling in Mechanobiology, 16*, 583-596.

Miyawaki, S., Tawhai, M., Hoffman, E. A., & Lin, C.-L. (2012). Effect of carrier gas properties on aerosol distribution in a CT-based human airway numerical model. *Annals of Biomedical Engineering, 40*, 1495-1507.

Moorman, J. E., Rudd, R. A., Johnson, C. A., King, P., Bailey, C., Scalia, M. R., & Akinbami, L. J. (2007). National surveillance of asthma - United States, 1980-2004. *Morbidity and Mortality Weekly Report: Surveillance Summaries, 56*, 1-54.

Morsi, S. A., & Alexander, A. J. (1972). An investigation of particle trajectories in two phase flow. *Journal of Fluid Mechanics, 55*, 193-208.

Newman, S. P. (2005). Principles of metered-dose inhaler design. *Respiratory Care, 50*, 1177-1190.

Newman, S. P., Weisz, A. W., Talaee, N., & Clarke, S. W. (1991). Improvement of drug delivery with a breath actuated pressurised aerosol for patients with poor inhaler technique. *Thorax, 46*, 712-716.

Nowak, N., Kakade, P. P., & Annapragada, A. V. (2003). Computational fluid dynamics simulation of airflow and aerosol deposition in human lungs. *Annals of Biomedical Engineering, 31*, 374-390.

Schlesinger, R. B., & Lippmann, M. (1978). Selective particle deposition and bronchogenic carcinoma. *Environmental Research, 15*(3), 424-431.

Schlesinger, R. B., Bohning, D. E., & Chan, T. L. (1977). Particle deposition in a hollow cast of the human tracheobronchial tree. *Journal of Aerosol Science, 8*(6), 429-445.

Son, Y., Longest, P. W., & Hindle, M. (2013). Aerosolization characteristics of dry powder inhaler formulations for the excipient enhanced growth (EEG) application: Effect of spray drying process conditions on aerosol performance. *International journal of Pharmaceutics, 443*, 137-145.

Tawhai, M. H., Hunter, P., Tschirren, J., Reinhardt, J., McLennan, G., & Hoffman, E. A. (2004). CT-based geometry analysis and finite element models of the human and ovine bronchial tree. *Journal of Applied Physiology, 97*, 2310-2321.

Tawhai, M. H., Pullan, A. J., & Hunter, P. J. (2000). Generation of an anatomically based three-dimensional model of the conducting airways. *Annals of Biomedical Engineering, 28*(7), 793-802.

Telko, M. J., & Hickey, A. J. (2005). Dry powder inhaler formulation. *Respiratory Care, 50*, 1209-1227.

Tian, G., Longest, P. W., Su, G., & Hindle, M. (2010). Characterization of respiratory drug delivery with enhanced condensational growth using an individual path model of the entire tracheobronchial airways. *Annals of Biomedical Engineering, 39*, 1136-1153.

Tsilingiris, P. T. (2008). Thermophysical and transport properties of humid air at temperature range between 0 and 100 C. *Energy Conversion & Management, 49*, 1098-1110.

Vreman, A. (2004). An eddy-viscosity subgrid-scale model for turbulent shear flow: Algebraic therory and applications. *Phys. Fluids, 16*, 3670-3681.

Walenga, R. L., & Longest, P. W. (2016). Current inhalers deliver very small doses to the lower tracheobronchial airways: Assessment of healthy and constricted lungs. *Journal of Pharmeceutical Sciences, 105*, 147-159.

Weibel, E. R. (1963). *Morphometry of the human lung.* New York: Academic.

Winkler-Heil, R., Ferron, G., & Hofmann, W. (2014). Calculation of hygroscopic particle deposition in the human lung. *Inhalation Toxicology, 26*, 193-206.

Wu, D., Miyawaki, S., Tawhai, M. H., Hoffman, E. A., & Lin, C.-L. (2015). A numerical study of water loss rate distributions in MDCT-based human airway models. *Annals of Biomedical Engineering, 43*, 2708-2721.

Xi, J., & Longest, P. W. (2008). Effects of oral airway geometry characteristics on the diffusional deposition of inhaled nanoparticles. *Journal of Biomechanical Engineering, 130*, 011008.

Yeh, H.-C., & Schum, G. M. (1980). Models of human lung airways and their application to inhaled particle deposition. *Bulletin of Mathematical Biology, 42*, 461-480.

Yin, Y., Choi, J., Hoffman, E. A., Tawhai, M. H., & Lin, C.-L. (2010). Simulation of pulmonary air flow with a subject-specific boundary condition. *Journal of Biomechanics, 43*, 2159-2163.

Yin, Y., Choi, J., Hoffman, E. A., Tawhai, M. H., & Lin, C.-L. (2013). A multiscale MDCT image-based breathing lung model with time varying regional ventilation. *Journal of Computational Physics, 244*, 168-192.

APPENDIX A: CHAPTER 1 NOMENCLATURE

MDI: Metered dose inhaler

DPI: Dry powder inhaler

CT: Computed tomography

SPECT: Single photon emission computed tomography

MDCT: Multiple detector computed tomography

MICA: Multiscale imaging-based cluster analysis

QCT: Quantitative computed tomography

CFD: Computational fluid dynamics

LMB: Left main bronchus

RMB: Right main bronchus

BronInt: Intermediate bronchus

TriLLB: Left lower lobe trifurcation

C1: Cluster 1

C2: Cluster 2

C3: Cluster 3

C4: Cluster 4

D_h^*: Normalized hydraulic diameter

θ_{RMB}: RMB bifurcation angle

TLC: Total lung capacity

FRC: Functional residual capacity

AirT%: Air trapping percentage of FRC

IC: Inspiratory capacity

HM: Healthy male

HF: Healthy female

LLL: Left lower lobe

SARP: Severe Asthma Research Program

TLC%: Percent predicted TLC

FRC%: percent predicted FRC

PI: Peak inspiration

PI/2: Half of peak inspiration

LES: Large eddy simulation

SGS: sub-grid scale

u_i: Fluid velocity vector, i component

x_i: Position vector, i component

ρ: Fluid density

p: Fluid pressure

ν: Fluid kinematic viscosity

ν_T: SGS small eddy fluid viscosity

T_{PIFR}: Time to peak inspiration flow rate

PIFR: Peak inspiration flow rate

Q: Flowrate

Re: Reynolds number

SEM: Synthetic eddy model

u_{pi}: Particle velocity vector, i component

F_D: Drag force on a particle

g_i: Gravity vector in the i component

ρ_p: Particle density

C_D: Drag coefficient

D_p: Particle diameter

Re_p: Particle Re

Stk: Stokes number

U_{mean}: Fluid mean velocity of current branch

C_c: Cunningham correction factor

D_b: Current airway branch diameter

μ: Fluid dynamic viscosity

DF: Deposition fraction

DE: Deposition efficiency

DD: Deposition density

$N_{p,ent}$: Number of particles entering a region

$N_{p,exit}$: Number of particles exiting a region

N_p: Number of particles released

SA: Surface area

RUL: Right upper lobe

RML: Right middle lobe

RLL: Right lower lobe

LUL: Left upper lobe

LLL: Left lower lobe

RUB: Right upper bronchus

ICS: Inhaled cortical steroid

y^+: Normalized averaged distance from the wall to first mesh element

APPENDIX B: CHAPTER 2 NOMENCLATURE

ϕ: Droplet diameter (m)

D_v^*: Modified molecular diffusivity of water, $^{m^2}/_{s}$

M_w: Molecular weight of water, $^{kg}/_{mol}$

R: Universal gas constant, $^{m^3 * Pa}/_{mol * K}$

ρ_d: Droplet density, $^{kg}/_{m^3}$

p_w: Density of water, $^{kg}/_{m^3}$

T_a: Ambient temperature, K

T_d: Droplet temperature, K

p^s: Water saturation pressure at ambient temperature, Pa

RH: Relative humidity, %

a_w: Water activity constant, unit less

$h_{f,g}$: Latent heat of condensation, $^{J}/_{kg}$

σ: Surface tension, $^{J}/_{m^2}$

δ_c: Non-continuum layer relative thickness, 2/3 (Broday & Georgopoulos, 2001)

λ: Mean free path of water in air, $7.12 * 10^{-8}$ (Broday & Georgopoulos, 2001)

α_c: Condensation coefficient, 1 (Broday & Georgopoulos, 2001)

α_t: Thermal accommodation coefficient, 0.3 (Broday & Georgopoulos, 2001)

ρ_a: Density of air, $^{kg}/_{m^3}$

c_p: Specific heat of air, $^{J}/_{kgK}$:

M_a: Molecular weight of air, $^{kg}/_{mol}$

k_v: Thermal conductivity of vapor-air mixture, $^{W}/_{mK}$

$c_{p,m}$: Specific heat of vapor-air mixture, $^{J}/_{kgK}$

$c_{p,w}$: Specific water, $^{J}/_{kgK}$

μ_v: Viscosity of water vapor